Shap. Mem. Superelasticity
https://doi.org/10.1007/s40830-022-00396-9

TECHNICAL ARTICLE

Coupled Finite Element Simulation of Shape Memory Bending Microactuator

Georgino Kaleng Tshikwand[1] · Lena Seigner[2] · Frank Wendler[1] · Manfred Kohl[2]

Received: 16 May 2022 / Revised: 30 September 2022 / Accepted: 30 September 2022

Abstract Due to their high-energy density, shape memory alloys (SMAs) are investigated as material for bending microactuators in applications of self-folding structures, realizing the concept of *programmable matter*. Here, for the numerical prediction of the electro-thermo-mechanical performance, the quantification of the time-dependent coupling effects in SMA materials during phase transformation is of crucial interest. Isothermal SMA material models cannot treat the time-dependent interaction between deformation, temperature and electric potential in thermally controlled actuation. In this paper, we extend an isothermal SMA model using standard thermodynamics (Coleman–Noll procedure) to treat the time-dependent behavior of polycrystalline SMAs. The model is implemented as a user material subroutine (UMAT) in a standard finite element (FE) code (Abaqus standard). The time-dependent loading of a tensile sample and a bending microactuator made from 20 μm thick SMA foil are simulated. A comparative study between experimental and simulation results on the thermoelastic and caloric effects during stress-induced phase transformation is presented. Joule heating simulations for shape recovery during both tensile and bending loading are conducted. Time-resolved temperature variations accompanying the loading and Joule heating processes are reported. The coupled SMA material model is found to be capable of approximating the time-dependent field quantities of a polycrystalline SMA microactuator subjected to electro-thermo-mechanical loading.

Keywords SMA modeling · Coupled FEM simulation · SMA microactuator · Bending actuation · Abaqus

This invited article is part of a special issue of Shape Memory and Superelasticity honoring Etienne Patoor for his contributions to the field of phase transforming materials and shape memory alloys. The special issue was organized by Dr. Fodil Meraghni, Ecole Nationale Supérieure d'Arts et Métiers (Arts et Métiers Institute of Technology), and Dr. Dimitris Lagoudas, Texas A&M University.

✉ Manfred Kohl
manfred.kohl@kit.edu

Georgino Kaleng Tshikwand
georgino.tshikwand@fau.de

Lena Seigner
lena.seigner@kit.edu

Frank Wendler
frank.wendler@fau.de

[1] Institute of Materials Simulation, Friedrich-Alexander University of Erlangen-Nürnberg (FAU), 90762 Fürth, Germany

[2] Institute of Microstructure Technology, Karlsruhe Institute of Technology, 76344 Eggenstein-Leopoldshafen, Germany

Introduction

For microsystem actuation, shape memory alloys (SMAs) offer desirable properties compared to other actuation materials. Nickel titanium (NiTi), since its discovery in 1962 [1, 2], has remained the most popular SMA to this day. NiTi shows attractive properties for actuation, amongst which are large stress and strain output, good damping, fatigue, corrosion properties and good biocompatibility [3–8]. Due to considerable progress in microtechnologies, NiTi thin film mechanical and medical microactuators gained large interest for various applications [9–11]. Examples of this research are the development of micropumps [12], microwrapper [13], microvalves [9, 14–16], heart valves [17]. For actuation, the conversion of thermal energy into mechanical energy can be achieved

Published online: 04 November 2022

through resistive heating related to the shape memory effect (SME). Promising application of thin film NiTi actuation can be anticipated for shape changing systems that are inspired from the Japanese art of paper folding, Origami [18]. Such an application requires bending actuation able to fold and unfold two dimensional (2D) planar structures into different three dimensional (3D) structures. Through the use of NiTi thin foils, 2D planar structures were programmed to self-fold to different 3D structures, for which the term programmable matter was coined [18]. The reduction in actuator size would allow for more complex 3D structures to be programmed [19]. However, as part of such developments, numerical simulations of the coupled electro-thermo-mechanical (CETM) behavior of the actuator need to be conducted. Design and performance analysis of NiTi microactuators can be achieved through finite element (FE) simulations. This provides information about optimal actuator geometries and limits for force-displacement or torque-angle output. As a prerequisite for such FE simulations, a material model describing the CETM behavior of SMA material need to be developed. Of all the material models describing the constitutive behavior of SMAs, fully thermomechanically coupled phenomenological SMA material models and other SMA constitutive models [20–30] have provided a close approximation of the physical behavior of SMA components. Developing phenomenological models, a thorough understanding the experimental behavior of SMA materials is crucial. Below, a short review on SMA behavior is presented. Shape memory alloys subscribe to a class of materials that show memory of the original shape after a thermomechanical deformation process. This process induces a crystallographic reversible solid–solid phase transformation between a high-temperature stable parent phase of austenite (A) and a low temperature stable martensite phase (M). Two main properties are related to this transformation, one-way shape memory effect (SME) and superelasticity (SE). SME is the thermomechanical process where a SMA sample at a certain initial temperature is cooled from the parent austenite phase to a twinned martensite phase without inducing shape change. Then the twinned martensite is subjected to a shape changing stress which reorient the twinned martensite phase to a de-twinned martensite. This process causes visible shape change in the sample. Heating the deformed sample to a temperature above the austenite finish temperature (A_f) recovers the original shape of the austenite phase. SE on the other hand is a mechanical process, where a sample in austenite configuration (temperature is above A_f) is loaded beyond the transformation stresses ($\sigma_{\mathrm{MS}}, \sigma_{\mathrm{MF}}$). This process induces a shape changing transformation from austenite to de-twinned martenite. Upon unloading, the sample recovers its original shape in austenite configuration. Figure 1 shows the stress–strain behavior of the one-way shape memory effect (SME) and superelasticity (SE).

Figure 2 shows the SMA phase diagram with the two aforementioned thermomechanical processes. The SMA material is a cold-rolled NiTi which exhibits a two-stage transformation between austenite and martensite via an intermediate phase, the so-called R-phase as detailed in our previous work [19]. Therefore, actuation at room temperature by Joule heating due to the shape memory effect involves R-phase transformation and stress-induced martensitic transformation depending on the stress level. These effects are approximated by the process depicted in Fig. 2.

The 3D isothermal thermomechanical material model presented in [28] describes both shape memory effect (SME) and superelasticity (SE) of SMA solid materials. It captures both thermally and stress-induced martensite variants and was applied recently for micro-bending actuators [19]. Compared to most phenomenological SMA material modeling approaches that use stress and temperature as control variable, the SMA material model presented here [28] assumes strain and temperature as control variables. From this assumption, a modified phase diagram (see Fig. 2) is generated and consequently the phase transformation is strain-controlled. The drawback of this work [28] is its isothermal setup, so time and spatially dependent electro-thermo-mechanical coupling effects occurring in SMA actuator devices are not tractable. However, these effects are crucial during device actuation. In the present paper, an extension of this model is presented to consider the coupling between mechanics, electric current flow and heat generation. This allows for a spatially and temporally resolved analysis of SMA microactuators.

The paper is structured as follows: The material model is briefly sketched, and a thermodynamical derivation of the heat dissipation terms is carried out, which are used in the heat balance equation. The kinetic equations for the temperature-coupled phase transformations are formulated. After a description of the implementation of the model in a finite element framework, we present comparisons of simulation results with experimental data on tensile and bending loading, and a simulation of the Joule-heated actuator performance.

Materials and Methods

Thermomechanical Modeling

As an elastic material with a nonlinear stress–strain relation, SMAs are often modeled as hypoelastic materials.

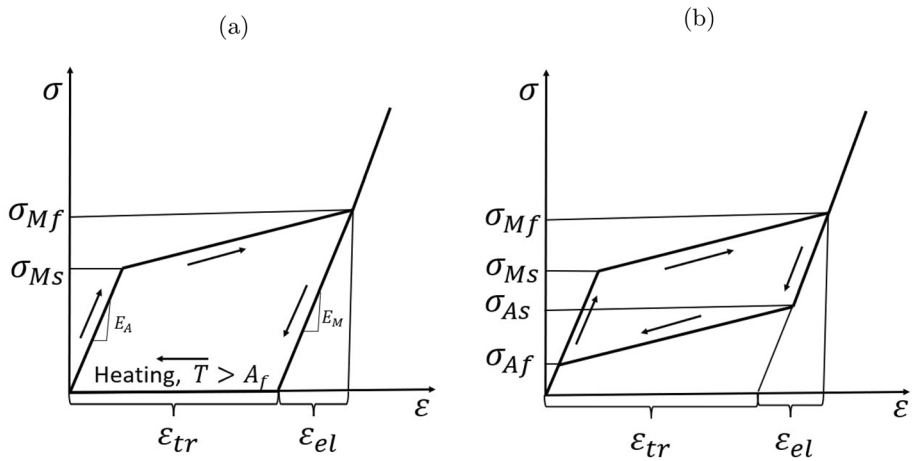

Fig. 1 Schematic stress–strain diagrams of SMAs: **a** one-way shape memory effect (SME); **b** superelasticity (SE)

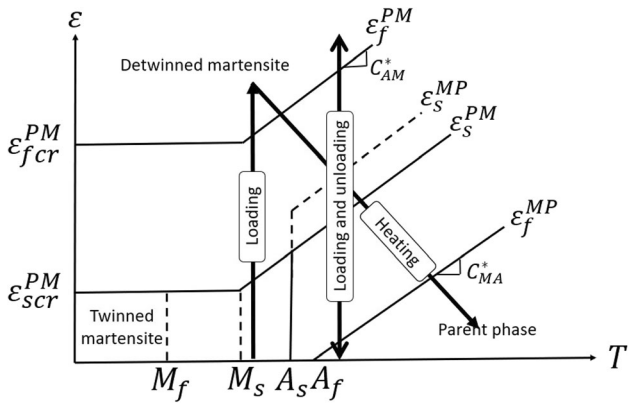

Fig. 2 Modified SMA phase diagram adapted from [28]

Rate additive hypoelastic formulation is assumed. Since the elastic strain is small compared to the transformation strain, the total strain rate tensor is additively decomposed into its elastic and transformation parts,

$$\dot{\varepsilon} = \dot{\varepsilon}_{\mathrm{el}} + \dot{\varepsilon}_{\mathrm{tr}} \tag{1}$$

As typical thermal expansion coefficients in NiTi are of the order of 10^{-5} K^{-1} (e.g. Table 2.5 in [31]) the thermal strain for the temperature changes during actuation of about 50 K is roughly two orders of magntitude smaller than the transformation strain. In this work, it will hence be neglected. The transformation strain is related to the progress in crystallographic phase transformation represented by the martensite volume fraction ξ, its direction being determined by the transformation tensor Λ. For the rate form of the transformation strain we choose

$$\dot{\varepsilon}_{tr} = \Lambda\,\dot{\xi}, \tag{2}$$

where the transformation tensor is defined as

$$\Lambda = \begin{cases} \varepsilon_{\mathrm{tr}}^{\max} \dfrac{\sigma'}{\|\sigma'\|} & \text{for} \quad \dot{\xi} > 0 \quad \text{(forward transformation)} \\ \varepsilon_{\mathrm{tr}}^{\max} \dfrac{\varepsilon_{\mathrm{tr}}}{\|\varepsilon_{\mathrm{tr}}\|} & \text{for} \quad \dot{\xi} < 0 \quad \text{(reverse transformation)} \end{cases} \tag{3}$$

Here, $\varepsilon_{\mathrm{tr}}^{\max}$ is the maximum transformation strain obtained from tensile testing experiments, and σ' is the deviatoric part of the stress tensor. Details about the isothermal SMA material model formulation can be found in [28].

In the following, we extend the model from [28] towards a thermomechanically coupled SMA model. Intensive studies have been conducted on the formulation of coupled problems in thermo-plasticity [32–34], on the material modelling and characterisation of shape memory alloys [14, 26, 27, 31, 35–38]. This vast knowledge base will serve as a reference to the formulation here. Following the Coleman–Noll procedure [39], constitutive equations will be derived. Assuming the validity of the framework of irreversible thermodynamics, we consider the thermal dissipation occurring during phase transformation described by the internal state variables ξ and $\varepsilon_{\mathrm{tr}}$ as a source of heat. The problem of a current-controlled actuator involves electric, thermal and mechanical processes, which for a continuum body are formulated by the conservation of electric charge, of linear momentum and of energy, respectively,

$$\begin{aligned} &\nabla \cdot \boldsymbol{J} = 0 \\ &\nabla \cdot \sigma = 0 \\ &\rho \dot{u} - \dot{w} + \nabla \cdot \boldsymbol{q} = 0, \end{aligned} \tag{4}$$

where $\boldsymbol{J}$ denotes the electrical current density, ρ the material density, u the specific internal energy, $\dot{w} = \sigma\dot{\varepsilon}$ the rate of specific mechanical work and $\boldsymbol{q}$ the heat flux. The Clausius–Duhem inequality as a version of the second law

of thermodynamics [40] states that in an irreversible process the entropy production is positive,

$$\rho T\dot{s} + \nabla \cdot \boldsymbol{q} - \boldsymbol{q} \cdot \frac{\nabla T}{T} \geq 0, \tag{5}$$

where s is the specific entropy, and T is the absolute temperature. Inserting Eqs. (4) into (5), a dissipation inequality is obtained, consisting of a mechanical dissipation, d_{mec}, and a thermal dissipation, d_{th},

$$d = [\rho T\dot{s} + \sigma\dot{\varepsilon} - \rho\dot{u}] + \left[-\mathbf{q} \cdot \frac{\nabla T}{T}\right] \geq 0 \tag{6}$$

Due to the choice of the strain tensor ε and temperature T as control variables, the thermodynamic state of the system is described by the specific Helmholtz free energy

$$\psi = \psi(\varepsilon, T, \varepsilon^{\text{tr}}, \xi) = u - sT, \tag{7}$$

with

$$\dot{\psi} = \dot{u} - \dot{s}T - s\dot{T} = \frac{\partial\psi}{\partial\varepsilon}\dot{\varepsilon} + \frac{\partial\psi}{\partial T}\dot{T} + \frac{\partial\psi}{\partial\varepsilon^{tr}}\dot{\varepsilon}^{tr} + \frac{\partial\psi}{\partial\xi}\dot{\xi}. \tag{8}$$

With Eq. (8), the dissipation inequality in terms of the Helmholtz free energy density is obtained from Eq. (6),

$$\sigma\dot{\varepsilon} - \rho s\dot{T} - \rho\frac{\partial\psi}{\partial\varepsilon}\dot{\varepsilon} - \rho\frac{\partial\psi}{\partial T}\dot{T} - \rho\frac{\partial\psi}{\partial\varepsilon^{tr}}\dot{\varepsilon}^{tr} - \rho\frac{\partial\psi}{\partial\xi}\dot{\xi} - \frac{1}{T}(\mathbf{q}\cdot\nabla T) \geq 0 \tag{9}$$

Fixing all state variables except one, fulfilling the inequality Eq. (9) requires

$$\begin{aligned} \sigma &= \rho\frac{\partial\psi}{\partial\varepsilon}, \\ s &= -\frac{\partial\psi}{\partial T}, \end{aligned} \tag{10}$$

which gives the constitutive equations for stress and entropy. Using Eqs. (10), (9) reduces to

$$\phi\dot{\varepsilon}^{\text{tr}} + \pi\dot{\xi} - \boldsymbol{q}\cdot\frac{\nabla T}{T} \geq 0, \tag{11}$$

where $\pi = -\rho\frac{\partial\psi}{\partial\xi}$, $\phi = -\rho\frac{\partial\psi}{\partial\varepsilon^{\text{tr}}}$ are the thermodynamic driving forces conjugate to the internal state variables, ξ and ε^{tr}, respectively. To satisfy Eq. (11), all terms should be positive. The term with the heat flux satisfies this condition using Fourier's law of heat conduction, $\boldsymbol{q} = -k\cdot\nabla T$, where k is an isotropic thermal conductivity tensor. The terms with the rate of internal state variables $\dot{\varepsilon}^{\text{tr}}$, $\dot{\xi}$ satisfy the inequality by considering a dissipation potential $\alpha(\pi, \phi; \xi, \varepsilon^{\text{tr}})$, with $\dot{\xi} = \frac{\partial\alpha}{\partial\pi}$ and $\dot{\varepsilon}^{\text{tr}} = \frac{\partial\alpha}{\partial\phi}$. The thermodynamic potential of the two component phenomenological model presented in [22, 23, 41–43] is selected. Converting the Gibbs free energy from the above mentioned work, the specific Helmholtz-free energy is obtained,

$$\begin{aligned} \psi(\varepsilon, T, \varepsilon^{\text{tr}}, \xi) = {} & \frac{1}{2\rho}\varepsilon : E : \varepsilon - \frac{1}{\rho}\varepsilon : E : \varepsilon^{\text{tr}} \\ & + c\left[(T - T_0) - T\ln\left(\frac{T}{T_0}\right)\right] \\ & - s_0 T + u_0, \end{aligned} \tag{12}$$

where E, c, s_0, and u_0 are the effective stiffness tensor, the effective specific heat, the effective specific entropy at the reference state, and the effective specific internal energy at the reference state, respectively. These material parameters are functions of the martensite volume fraction, ξ, and they are defined below using a mixture rule,

$$\begin{aligned} E(\xi) &= E^A + \xi\left(E^M - E^A\right) = E^A + \xi\Delta E \\ c(\xi) &= c^A + \xi\left(c^M - c^A\right) = c^A + \xi\Delta c \\ s_0(\xi) &= s_0^A + \xi\left(s_0^M - s_0^A\right) = s_0^A + \xi\Delta s_0 \\ u_0(\xi) &= u_0^A + \xi\left(u_0^M - u_0^A\right) = u_0^A + \xi\Delta u_0 \end{aligned} \tag{13}$$

The superscript $()^A$ and $()^M$ refer to the austenite and martensite phases, respectively. Using Eqs. (10), (12) and (13), the Coleman–Noll procedure gives the following constitutive equations,

$$\begin{aligned} \sigma &= \rho\frac{\partial\psi}{\partial\varepsilon} = E : (\varepsilon - \varepsilon^{tr}), \\ s &= -\frac{\partial\psi}{\partial T} = c\ln\left(\frac{T}{T_0}\right) + s_0, \\ \phi &= -\rho\frac{\partial\psi}{\partial\varepsilon^{tr}} = E : \varepsilon, \\ \pi &= -\rho\frac{\partial\psi}{\partial\xi} = -\frac{1}{2}\varepsilon : \Delta E : \varepsilon + \varepsilon : \Delta E : \varepsilon^{tr} \\ & \quad - \rho\Delta c\left[(T - T_0) - T\ln\left(\frac{T}{T_0}\right)\right] \\ & \quad + \rho\Delta s_0 T - \rho\Delta u_0 \end{aligned} \tag{14}$$

Volumetric Heat Dissipation Due to Phase Transformation

There is a release of heat during the solid–solid phase transformation of an SMA component subjected to a thermomechanical deformation process. In order to quantify this energy, the entropy production during this process is considered. Using the evolution of internal energy from Eq. (4) and that of the free energy from Eq. (8), an expression of the entropy production is obtained,

$$\rho T\dot{s} = \rho r - \nabla\cdot\boldsymbol{q} - \rho\frac{\partial\psi}{\partial\varepsilon^{\text{tr}}}\dot{\varepsilon}^{\text{tr}} - \rho\frac{\partial\psi}{\partial\xi}\dot{\xi} \tag{15}$$

Depending on the strain rate, local heat dissipation in SMA becomes considerable. Given the dependence of mechanical properties on temperature, this phenomenon is important for SMA time-dependent actuators. This enforces the need for a coupled thermo-mechanical material model.

Using Eq. (14), the entropy production takes the form,

$$\begin{aligned}\rho T\dot{s} &= -T\frac{\mathrm{d}}{\mathrm{d}t}\left(\rho\frac{\partial\psi}{\partial T}\right)\\ &= -T\left(\rho\frac{\partial^2\psi}{\partial T\partial\varepsilon}\dot{\varepsilon}+\rho\frac{\partial^2\psi}{\partial T^2}\dot{T}+\rho\frac{\partial^2\psi}{\partial T\partial\varepsilon^{\mathrm{tr}}}\dot{\varepsilon}^{\mathrm{tr}}+\rho\frac{\partial^2\psi}{\partial T\partial\xi}\dot{\xi}\right)\end{aligned} \tag{16}$$

Equating Eqs. (15) to (16),

$$\begin{aligned}&-T\frac{\partial\sigma}{\partial T}\dot{\varepsilon}+T\rho\frac{\partial s}{\partial T}\dot{T}+T\frac{\partial\phi}{\partial T}\dot{\varepsilon}^{tr}+T\frac{\partial\pi}{\partial T}\dot{\xi}\\ &\quad=\rho r-\nabla\cdot\boldsymbol{q}-\rho\frac{\partial\psi}{\partial\varepsilon^{tr}}\dot{\varepsilon}^{tr}-\rho\frac{\partial\psi}{\partial\xi}\dot{\xi}\end{aligned} \tag{17}$$

here $T\frac{\partial s}{\partial T}=c$, where c is the specific heat capacity. From Eqs. (6) and (8), using definitions in Eq. (14), the mechanical or transformation dissipation becomes $d_{\mathrm{mec}}=-\rho\frac{\partial\psi}{\partial\varepsilon^{tr}}\dot{\varepsilon}^{\mathrm{tr}}-\rho\frac{\partial\psi}{\partial\xi}\dot{\xi}$. With this definition, Eq. (17) becomes,

$$-T\frac{\partial\sigma}{\partial T}\dot{\varepsilon}+\rho c\dot{T}+T\frac{\partial\phi}{\partial T}\dot{\varepsilon}^{\mathrm{tr}}+T\frac{\partial\pi}{\partial T}\dot{\xi}=\rho r-\nabla\cdot\boldsymbol{q}+d_{\mathrm{mec}} \tag{18}$$

Using Fourier's law, a heat equation can be obtained from Eq. (18),

$$\begin{aligned}\rho c\dot{T}-\nabla\cdot(k\nabla T)&=\rho r+T\frac{\partial\sigma}{\partial T}\dot{\varepsilon}\\ &\quad-T\frac{\partial\phi}{\partial T}\dot{\varepsilon}^{\mathrm{tr}}-T\frac{\partial\pi}{\partial T}\dot{\xi}+d_{\mathrm{mec}}\end{aligned} \tag{19}$$

In the heat Eq. (19), $-T\frac{\partial\pi}{\partial T}\dot{\xi}+d_{\mathrm{mec}}$ is the term coupling the mechanical field and thermal field, responsible for the volumetric heat dissipation during phase transformation, acting as an extra heat source in the heat equation. It can also be concluded from Eq. (14) that,

$$\begin{aligned}&\rho T\frac{\partial\sigma}{\partial T}\dot{\varepsilon}=0\\ &T\frac{\partial\phi}{\partial T}\dot{\varepsilon}^{\mathrm{tr}}=0\\ &T\frac{\partial\pi}{\partial T}\dot{\xi}=\left(-\rho\Delta cT\ln\left(\frac{T}{T_0}\right)+\rho\Delta s_0T\right)\dot{\xi}\\ &d_{\mathrm{mec}}=\{\varepsilon:\Delta E\}:\dot{\varepsilon}^{\mathrm{tr}}+\left\{-\frac{1}{2}(\varepsilon:\Delta E:\varepsilon)+\varepsilon:\Delta E:\varepsilon^{\mathrm{tr}}\right.\\ &\qquad\left.-\rho\Delta c\left[(T-T_0)-T\ln\left(\frac{T}{T_0}\right)\right]+\rho\Delta s_0T-\rho\Delta u_0\right\}\cdot\dot{\xi}\end{aligned} \tag{20}$$

Joule Heating

For actuation by Joule heating a current density J passing through the SMA acts as an additional heat source, driven by an electric field E, which is the negative gradient of the electric potential. This creates a coupling between the thermal field and electric field through the resistive heating or Joule's effect. The local electrical power released as heat is then

$$\begin{aligned}&H_{\mathrm{elec}}=E\cdot J,\quad\text{with}\\ &J=\sigma^{\mathrm{el}}(T)E\\ &E=-\frac{\partial v}{\partial x},\end{aligned} \tag{21}$$

where σ^{el} is a temperature-dependent electrical conductivity and v is the electrical potential. It is evident that the constitutive behavior of the flow of electric current density expressed in Eq. (21) is inserted in the conservation of electric charge in order to find a numerical solution for the electric potential. The final form of the heat equation is found by replacing ρr by H_{elec} in Eq. (19),

$$\rho c\dot{T}-\nabla\cdot(k\nabla T)=H_{\mathrm{elec}}-T\frac{\partial\pi}{\partial T}\dot{\xi}+d_{\mathrm{mec}} \tag{22}$$

Equations (14) and (22) are required equations governing the deformation, heat conduction , and resistive heating of SMA materials. A convection boundary condition is considered for the solid's surface,

$$H_{\mathrm{convec}}=-h(T_{\mathrm{surf}}-T_{\mathrm{amb}}) \tag{23}$$

where h is the convective heat transfer coefficient or film coefficient, T_{surf} is the solid surface temperature and T_{amb} is the ambient temperature.

Evolution of Internal State Variables

The detailed description of the relationship between the transformation strain tensor and the martensite volume fraction is found in [28]. Only the important points related to the kinetic law are mentioned in this section. First, a definition of the parameters of the modified phase diagram and state functions is important. The parameters of the phase diagram define the limits of the internal phase transformations. For the forward transformation, from the parent phase, P, to the martensite phase, M, we have,

$$\begin{aligned}\varepsilon_s^{\mathrm{PM}}&=\frac{\sigma_s^{PM}}{E_{\mathrm{mix}}}+\xi\cdot\varepsilon_{\max}^{\mathrm{tr}}\\ \varepsilon_f^{\mathrm{PM}}&=\frac{\sigma_f^{\mathrm{PM}}}{E_m}+\varepsilon_{\max}^{\mathrm{tr}}\end{aligned} \tag{24}$$

and for the reverse transformation, the martensite phase to back to the parent phase,

$$\varepsilon_s^{\mathrm{MP}} = \frac{\sigma_s^{\mathrm{MP}}}{E_{\mathrm{mix}}} + \xi \cdot \varepsilon_{\mathrm{max}}^{\mathrm{tr}}$$
$$\varepsilon_f^{\mathrm{MP}} = \frac{\sigma_f^{\mathrm{MP}}}{E_p} + \varepsilon_{\mathrm{max}}^{\mathrm{tr}} \tag{25}$$

where the subscript s and f denote start and finish. In ABAQUS standard, within the framework of finite strain theory, the strain tensor is defined as an integral of the deformation rate D, which is equivalent to the logarithmic strain (see Sect. 1.2.2 of ABAQUS Analysis User's Manual [44]) when the deformation rate is in a corotational cartesian space [45]. The integral is evaluated using the algorithm proposed in [46] and an incremental integration scheme based on the objective Jaumann rate of the cauchy stress is carried out (see Sects. 1.5.3 and 3.2.2 of ABAQUS Theory Manual [44]).

For the strain tensor this means,

$$\varepsilon_{n+1} = \Delta R \cdot \varepsilon_n \,.\, \Delta R^{\mathrm{T}} + \Delta\varepsilon$$
$$\Delta\varepsilon = \int_n^{n+1} D\,\Delta t \tag{26}$$

where ε_{n+1} and ε_n refer to the strain tensor a time step $t + \Delta t$ and t, respectively, $\Delta\varepsilon$ refer to the strain increment, and ΔR is the incremental rotation which brings the strain tensor in the current frame of reference to ensure material objectivity.

Considering this aspect, the state function for the forward transformation, $\varepsilon^{\mathrm{PM}}$, and the reverse transformation, $\varepsilon^{\mathrm{MP}}$, are defined in incremental form as,

$$\varepsilon_n^{\mathrm{PM}} = \varepsilon_{\mathrm{eq}} + C^{\mathrm{PM}} \frac{T - T_{\mathrm{ref}}}{E_{\mathrm{mix}}}$$
$$\varepsilon_{n+1}^{\mathrm{PM}} = \varepsilon_{\mathrm{eq}} + \Delta\varepsilon_{eq}$$
$$\varepsilon_n^{\mathrm{MP}} = \varepsilon_{\mathrm{eq}} + C^{\mathrm{PM}} \frac{T - T_{\mathrm{ref}}}{E_{\mathrm{mix}}}$$
$$\varepsilon_{n+1}^{\mathrm{MP}} = \varepsilon_{\mathrm{eq}} + \Delta\varepsilon_{\mathrm{eq}} \tag{27}$$

All the conditions above are considered for temperature above the martensite start temperature, $T > M_s$, relevant to the application for SMA actuation. The martensite volume fraction and the transformation strain tensor are computed for both forward and reverse transformations following Algorithm 1,

Algorithm 1 Forward and Reverse Transformations

Forward Transformation (Thermo-Mechanical process)
if $T > M_s$ **then**
  if $\varepsilon_{n+1}^{PM} > \varepsilon_s^{PM}$ **then**
    $\Delta\xi_{n+1} = (1-\xi_n)\frac{\varepsilon_{n+1}^{PM} - \varepsilon_s^{PM}}{\varepsilon_f^{PM} - \varepsilon_s^{PM}}$
    $\Delta\varepsilon_{n+1}^{tr} = \Delta\xi_{n+1} \cdot \varepsilon_{max}^{tr} \cdot \frac{\varepsilon}{\varepsilon'}$
    $\xi_{n+1} = \xi_n + \Delta\xi_{n+1}$
    $\varepsilon_{n+1}^{tr} = \varepsilon_n^{tr} + \Delta\varepsilon_{n+1}^{tr}$
  end if
end if
Reverse Transformation (Electro-Thermo-Mechanical process)
if $T > A_s$ **then**
  if $\varepsilon_{n+1}^{MP} < \varepsilon_s^{MP}$ **then**
    $\Delta\xi_{n+1} = -\xi_n \frac{\varepsilon_{n+1}^{MP} - \varepsilon_s^{MP}}{\varepsilon_f^{MP} - \varepsilon_s^{MP}}$
    $\Delta\varepsilon_{n+1}^{tr} = \frac{\Delta\xi_{n+1}}{\xi_n} \cdot \varepsilon_n^{tr}$
    $\xi_{n+1} = \xi_n + \Delta\xi_{n+1}$
    $\varepsilon_{n+1}^{tr} = \varepsilon_n^{tr} + \Delta\varepsilon_{n+1}^{tr}$
  end if
end if

Following an incremental analysis, these internal state variables are computed and saved in the UMAT variable STATEVs.

Implementation and Algorithms

The governing partial differential equations describing the mechanical, thermal, and electrical problems presented in Eqs. (4) and (22) are in their strong forms, and not suitable to be solved numerically.They are mostly solved using the finite element method (FEM). It is important to note that to include large displacement and large rotation in the kinematics of the finite elements, the mechanical equation is approximated using an updated Lagrangian formulation. Details about this formulation and its effectiveness are reported in [47, 48]. The cumbersome notation to signify that the integral form considers an updated Lagrangian formulation have not been included. However, the stress measure in this formulation is that of the Jaumann–Cauchy stress, $\boldsymbol{\sigma}$. Only discretized equations are reported here, the general formulation can be found in Appendix 1. The discretized finite element equations, considering no body force, and no internal current source, are

$$\begin{aligned}
&\int_V \nabla N^a(x) \cdot \boldsymbol{\sigma}(\varepsilon)\, \mathrm{d}V - \int_S N^a(x)\, \boldsymbol{\sigma} \cdot \mathbf{n}\, \mathrm{d}S = 0 \\
&\int_V \nabla N^a(x) \cdot (\mathbf{q})\, \mathrm{d}V + \int_S N^a(x)\, \mathbf{q}.\mathbf{n}\, \mathrm{d}S \\
&\quad - \int_V N^a(x)\, \rho c \left(\frac{T^{t+\Delta t} - T^t}{\Delta t} \right) \mathrm{d}V + \int_V N^a(x)\, H_{\text{elec}}\, \mathrm{d}V \\
&\quad - \int_V N^a(x)\, N^a(x) T^a \frac{\partial \pi}{\partial T} \left(\frac{\xi^{t+\Delta t} - \xi^t}{\Delta t} \right) \mathrm{d}V \\
&\quad + \int_V N^a(x)\, d_{\text{mec}}\, \mathrm{d}V = 0 \\
&\int_V \nabla N^a(x) \cdot \boldsymbol{J}\, \mathrm{d}V + \int_S N^a(x)\, \mathbf{J} \cdot \mathbf{n}\, \mathrm{d}S = 0
\end{aligned} \tag{28}$$

Using the commercial finite element solver Abaqus Standard, a combination of user subroutines UMAT and UMATH [44] are used to implement the constitutive material model. The subroutine UVARM is also used to access the electrical energy density, which is used in the UMAT subroutine with the help of common blocks, a useful feature in the FORTRAN 77 programming language. The source term to the heat equation are passed in the variable *RPL* to define the coupling between the displacement and the temperature and between the temperature and the electric potential, as detailed in [44].

Tangent Stiffness Tensor, UMAT Variable DDSDDE

As reported in Sect. 1.1.31 of the ABAQUS User Subroutines Reference Manual [44], the tangent stiffness matrix, $DDSDDE(I,J) = \frac{\partial \Delta\sigma}{\partial \Delta\epsilon}$, where $\Delta\sigma$, and $\Delta\epsilon$ are the stress and strain increments, defines the change in the I^{th} stress component at the end of the time increment caused by an infinitesimal perturbation of the J^{th} component of the strain increment array. Deriving the tangent stiffness matrix stipulate finding a relationship between the variation in the stress increment and that of the strain increment. The SMA constitutive model can be written in incremental form as follows,

$$\mathrm{d}\sigma = E_T : \mathrm{d}\varepsilon \tag{29}$$

where E_T is the required tangent stiffness tensor. Writing the constitutive relation from Eq. (14) in differential form gives,

$$\mathrm{d}\sigma = E : (\mathrm{d}\varepsilon - \mathrm{d}\varepsilon_{tr}) + \mathrm{d}\xi\, \Delta E\, (\varepsilon - \varepsilon_{\text{tr}}) \tag{30}$$

Using Eqs. (29) and (30) an expression for the tangent stiffness tensor E_T can be obtained and saved in the UMAT variable *DDSDDE* for the solution of 3D continuum FEM problem.

Return Mapping Algorithm

The return mapping algorithm or the implicit Euler method is a numerical integration scheme used to solve rate-dependent governing equations [45, 49]. This method consists of two steps, the elastic-predictor and transformation-corrector. This algorithm is implemented in [28]. We re-write it with respect the new coupled model to include the incremental computation of the coupling terms during transformation and the new stress–strain relation as seen in Algorithm 2.

Algorithm 2 Return-mapping Algorithm

$\varepsilon_n,\ \sigma_n,\ T_n,\ \xi_n,\ \varepsilon_n^{tr},\ \Delta\varepsilon_n,\ \Delta T_n,\ rpl_n$ are given at time step t_n
Assuming $\Delta\xi_n = 0,\ \Delta\varepsilon_n^{tr} = 0,\ \Delta rpl_n = 0,$ No Transformation
Elastic predictor
Compute elastic trial state
$\Delta\varepsilon_{n+1}^{trial} = \Delta\varepsilon_n$
$\varepsilon_{n+1}^{trial} = \varepsilon_n + \Delta\varepsilon_{n+1}^{trial}$
$\varepsilon_{n+1}^{PM} = \varepsilon_{eq} + \Delta\varepsilon_{eq}$
$\Delta\sigma_{n+1}^{trial} = E_{el} : \Delta\varepsilon_{n+1}^{trial}$
Transformation-corector
Check for transformation (refer to algorithm 1 for complete checks for both transformations)
if $\varepsilon_{n+1}^{PM} > \varepsilon_s^{PM}$ **then**
Transformation occurs, Compute $\Delta\xi_{n+1},\ \Delta\varepsilon_{n+1}^{tr},\ \xi_{n+1}, and\ \varepsilon_{n+1}^{tr},\ \Delta rpl_{n+1}$
  $\Delta\xi_{n+1} = (1-\xi_n)\frac{\varepsilon_{n+1}^{PM} - \varepsilon_s^{PM}}{\varepsilon_f^{PM} - \varepsilon_s^{PM}}$
  $\Delta\varepsilon_{n+1}^{tr} = \Delta\xi_{n+1} \cdot \varepsilon_{max}^{tr} \cdot \frac{\varepsilon}{\varepsilon'}$
  $\xi_{n+1} = \xi_n + \Delta\xi_{n+1}$
  $\varepsilon_{n+1}^{tr} = \varepsilon_n^{tr} + \Delta\varepsilon_{n+1}^{tr}$
Correct $\Delta\sigma_{n+1}^{trial}$ to get $\Delta\sigma_{n+1}$
Compute
  $\sigma_{n+1} = \sigma_n + \Delta\sigma_{n+1}$
Assuming $c^A = c^M, \Delta c = 0$
  $\Delta rpl_{n+1} = \{-0.5 \cdot (\varepsilon_{n+1} : \Delta E : \varepsilon_{n+1}) - (\varepsilon_{n+1} : \Delta E : \varepsilon_{n+1}^{tr}) + \rho\Delta u_0\} \cdot \Delta\xi_{n+1} + E : \varepsilon_{n+1} : \Delta\varepsilon_{n+1}^{tr}$
  $rpl_{n+1} = rpl_n + \Delta rpl_{n+1}$
else
No transformation
end if
Outputs
$\sigma_{n+1},\ \varepsilon_{n+1},\ \varepsilon_{n+1}^{tr},\ \xi_{n+1},\ \Delta rpl_{n+1},\ rpl_{n+1}\ T_{n+1},$

The algorithm is applied until the total external load has been incrementally applied.

Results and Discussion

Examples are presented to show the efficiency of the material model. First, tensile test simulation results of 20 µm thin NiTi tensile samples are presented for model validation. Then, bending simulation of 20 µm thin NiTi microactuators are presented. An unidirectional actuation simulation is finally presented at the end of this section. CAD geometries with sample dimensions used for the simulation can be found in Appendix 2. Input parameters to the model are summarized in Appendix 3. Mechanical properties were collected from our previous work [19]. Thermal properties were taken from a study on the investigation of sputter-deposited TiNiCuCo thin films [50] and

for the convection coefficient, the value is approximated from a study presented for a SMA wire [51]. Temperature-dependent electrical conductivity was measured with our in-house devices as seen in Fig. 21 in Appendix 2.

Tensile Simulations

First, uniaxial tensile loading simulations were carried out to evaluate the thermoelastic and caloric effects during phase transformation of a 20 µm thin tensile sample as seen in Fig. 17 in Appendix 2. The simulation is displacement controlled. One end of the sample is fixed while the other is stretched to induce a total strain of 6%. To represent the experimental tensile test closely, both ends of the sample are kept at room temperature. A heat convection condition is applied on the sample's outer film surfaces. The same strain rate was used during loading and unloading process.

Experimentally, to observe such caloric effects for thin structures, a high strain rate test is required. Two strain rates used for experimental tensile tests were simulated. The stress-strain behavior and temperature effects are reported in Figs. 3 and 4.

As the transformation initiates during the loading process, there is a rise in temperature due to the latent heat of stress-induced transformation. As a result, the transformation stress increases. The opposite effect occurs during the unloading process. The strain rate has a considerable effect on the transformation temperature as the transformation progresses. Experimentally, average temperature changes of approximately 10 K and 6 K (see Fig. 4) were recorded for strain rates of 5×10^{-2} s^{-1} and 1×10^{-2} s^{-1} respectively. Simulations show the same trend, the strain rate 5×10^{-2} s^{-1} shows an over-estimation in the approximation of the experimental results. The discrepancy between experimental and simulated temperature profiles depends on the strain rate. For a strain rate of 1×10^{-2} s^{-1}, we obtain an acceptable approximation of the experimental result with maximum simulated value of 306.5 K compared to maximum experimental value of 304.8 K. However, the detailed time-depended courses of local average temperature differ from each other. This difference is attributed to the complex dynamics of stress-induced phase transformation including local overheating due to formation of strain bands [52], which is not considered in the presented model. Furthermore, heat transfer strongly depends on the

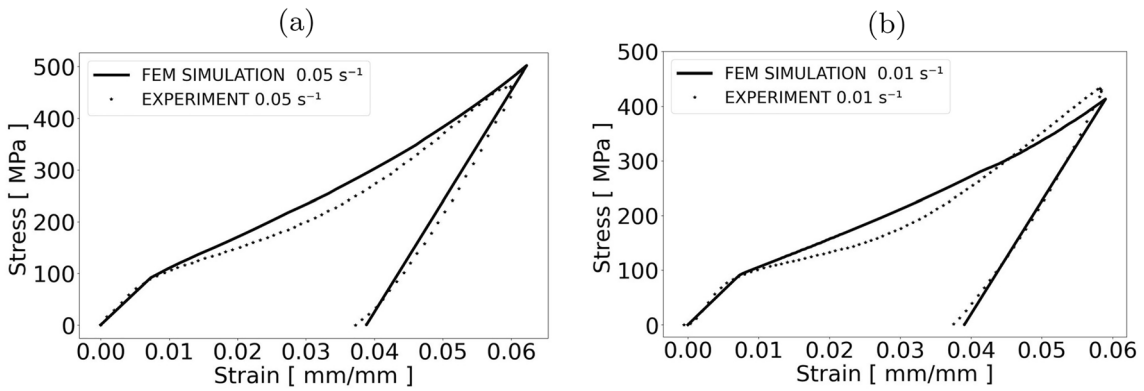

Fig. 3 Comparison of the strain rate effects on the experimental and simulated stress–strain behavior of a 20 µm thin NiTi tensile sample ($T_{\text{ref}} = 299\,K$), **a** strain rate 5×10^{-2} s^{-1}, **b** strain rate 1×10^{-2} s^{-1}

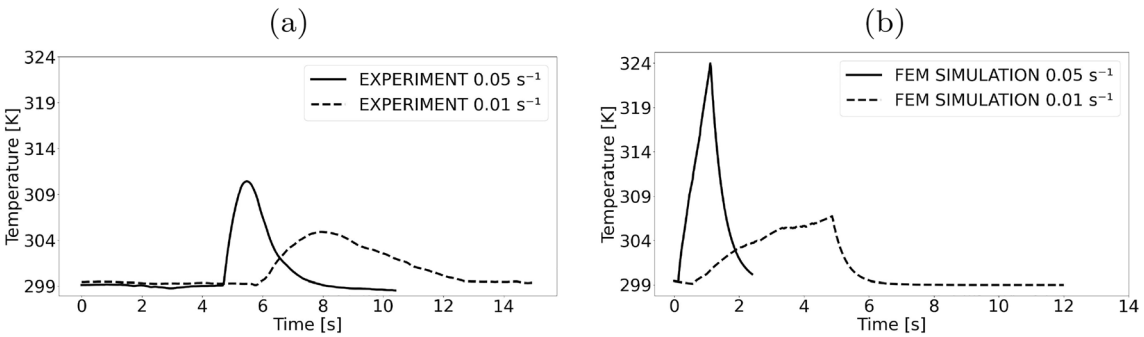

Fig. 4 Time-resolved local average temperature variation during stress-induced phase transformation of a 20 µm thin NiTi tensile sample ($T_{\text{ref}} = 299\,K$): **a** experiment; **b** FEM simulation

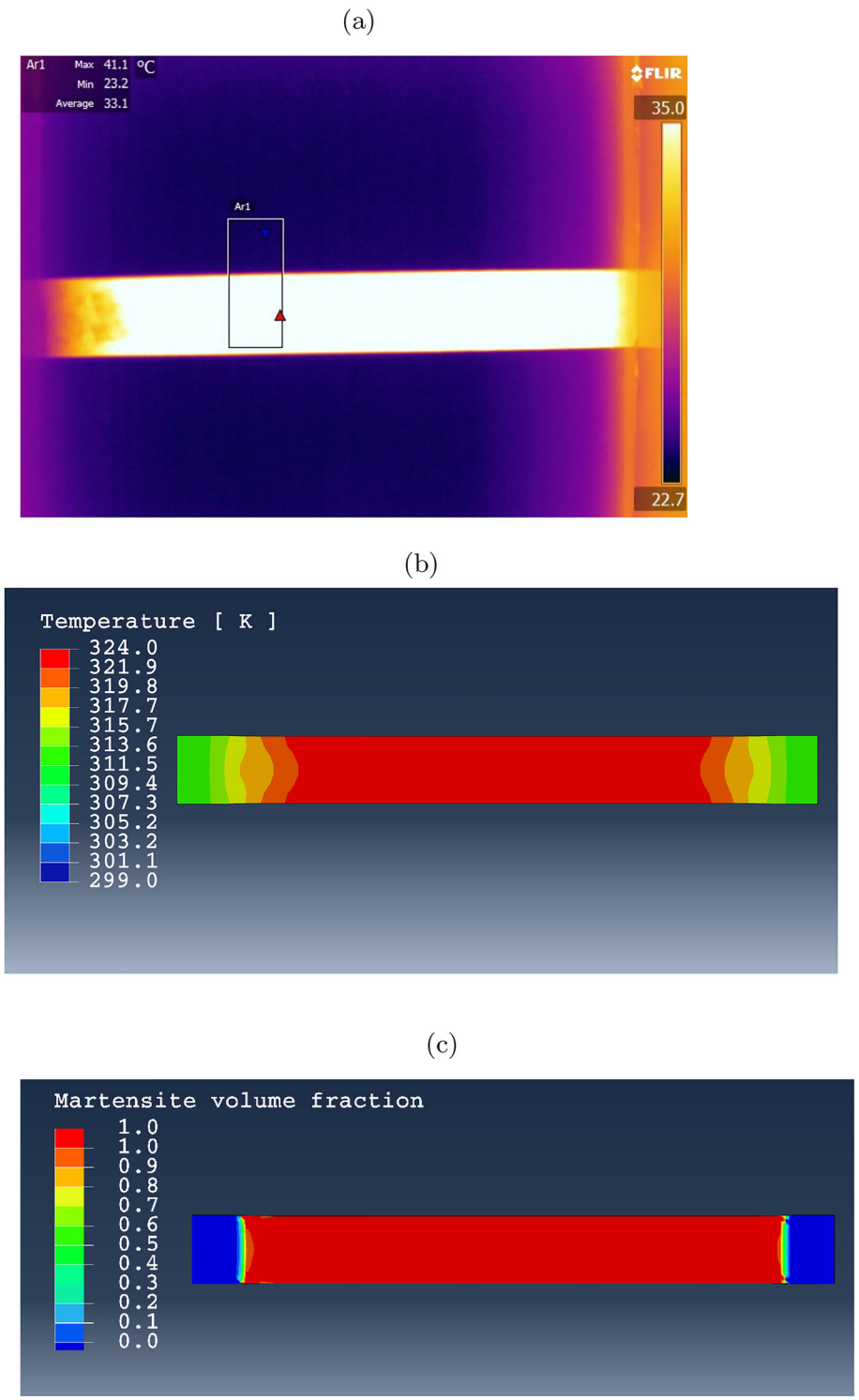

Fig. 5 Comparison of simulation and measurements during stress-induced phase transformation of a 20 µm thin NiTi tensile sample (strain rate: 5×10^{-2} s^{-1}, $T_{\text{ref}} = 297$ K): **a** experimental temperature map with $T_{\text{max}} = 314.3$ K when fully loaded; **b** simulated temperature map with $T_{\text{max}} = 324.0$ K when fully loaded, **c** simulated martensite fraction

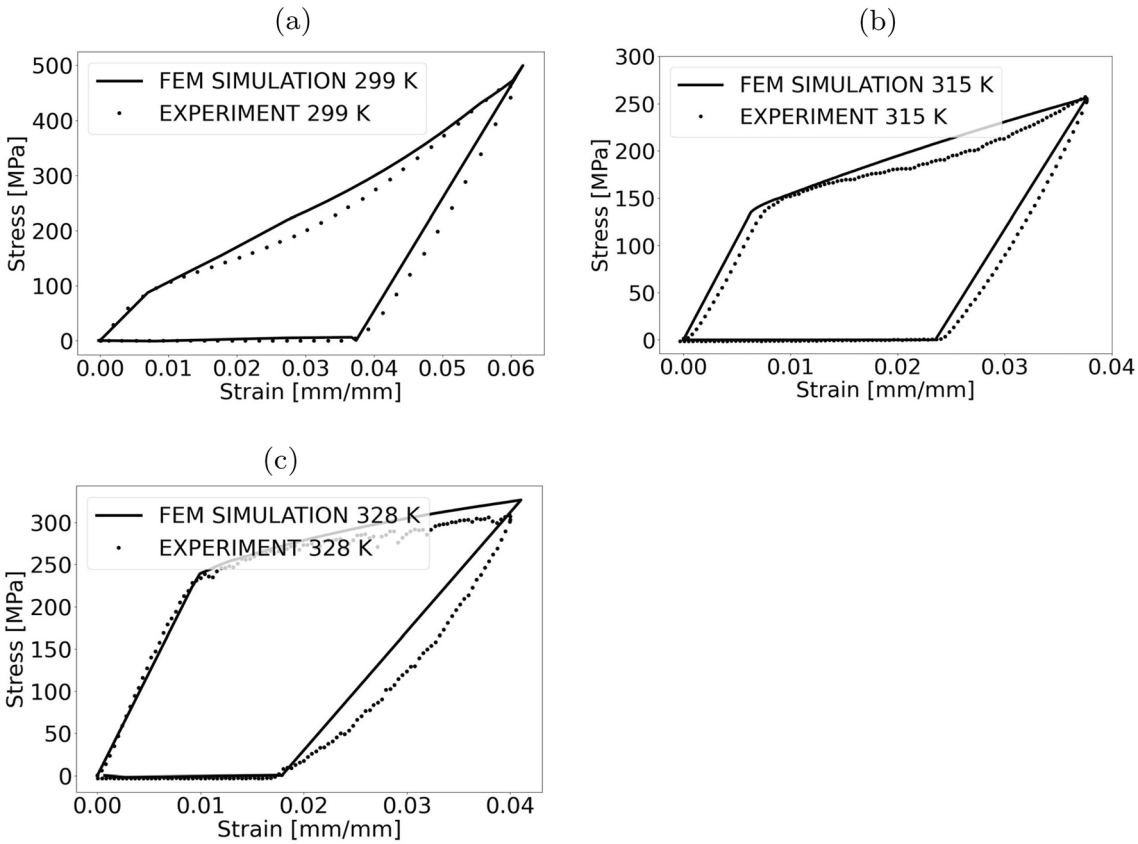

Fig. 6 Comparison of the experimental and simulation stress-strain results for full loading–unloading-Joule heating for reference temperatures: **a** 299 K, **b** 315 K, **c** 328 K

phase-fraction-dependent thermal conductivity as well as heat convection, which is approximated here using thermal characterization data from literature [51]. For a strain rate of 5×10^{-2} s^{-1}, these differences become even more pronounced.

Figure 5a shows an infrared (IR) temperature profile during the tensile loading. A corresponding profile from the simulation of the tensile loading can be seen in Fig. 5b. The maximum temperature reached during loading is 314 K and 324 K for the experimental and simulation result, respectively. The distribution of martensite volume fraction responsible for the rise in temperature can be seen in Fig. 5c, when fully loaded. The region in the grips at both ends of the sample do not show transformation. The temperature in this region rises due to heat conduction from the transformed region of the tensile sample.

Next, the full loading–unloading-Joule heating simulation is carried out for different reference temperatures. This consists of a loading step, whereby the sample is loaded until the total strain is induced. Then, an unloading step follows, whereby the sample is elastically unloaded, $\varepsilon_{\text{el}} = 0$. Finally, the sample is Joule heated above the austenite finish temperature to recover the induced transformation strain, $\varepsilon_{\text{tr}} = 0$. The tensile simulations are conducted at strain rates of 5×10^{-2} s^{-1}, 1×10^{-4} s^{-1}, and 1×10^{-4} s^{-1} for 299 K, 315 K, and 328 K reference temperatures, respectively. The simulation time periods, to induce an approximate total strain of 0.06, 0.0377, 0.04, for such strain rates is 1.2, 377, and 410 s, respectively. Joule heating for all three reference temperatures is carried out by passing an electric current through the sample within 10 s. Figure 6 shows the comparison of the experimental and simulation stress strain results.

As seen in Fig. 6, the transformation strain induced is approximately 3.7%, 2.35%, and 1.78% for the 299 K, 315 K, and 328 K reference temperatures, respectively. With Joule heating, the accumulated martensite fraction and transformation strain decrease as the local temperature incrementally increases. Figures 7 and 8 show time-resolved FEM simulations of Joule heating and its effects on the temperature, martensite fraction, and transformation strain for different reference temperatures. The Joule heating simulation lasts for 10 s. An electric current of 0.84 A is passed through the sample causing an increase in the sample local temperature because of the Joule effect.

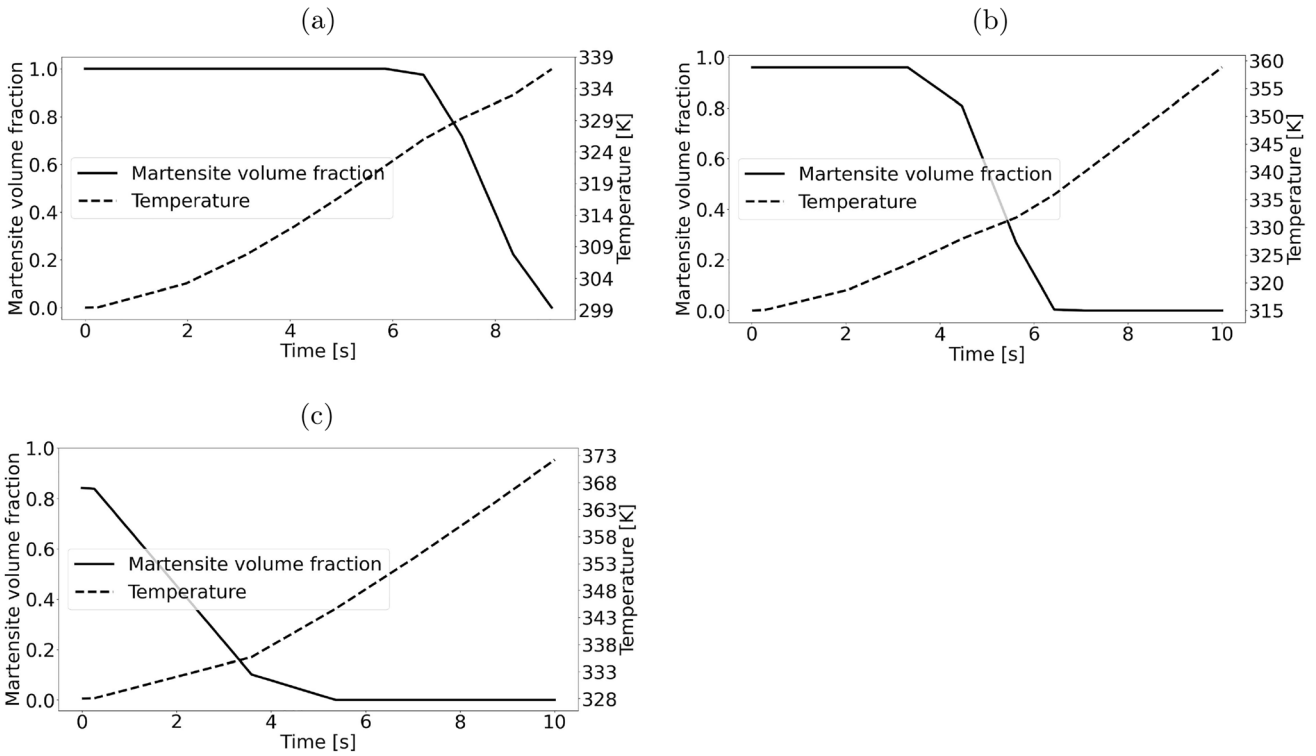

Fig. 7 Time-resolved FEM simulation of Joule heating and its effects on the temperature and martensite fraction for reference temperatures: **a** 299 K, **b** 315 K, **c** 328 K

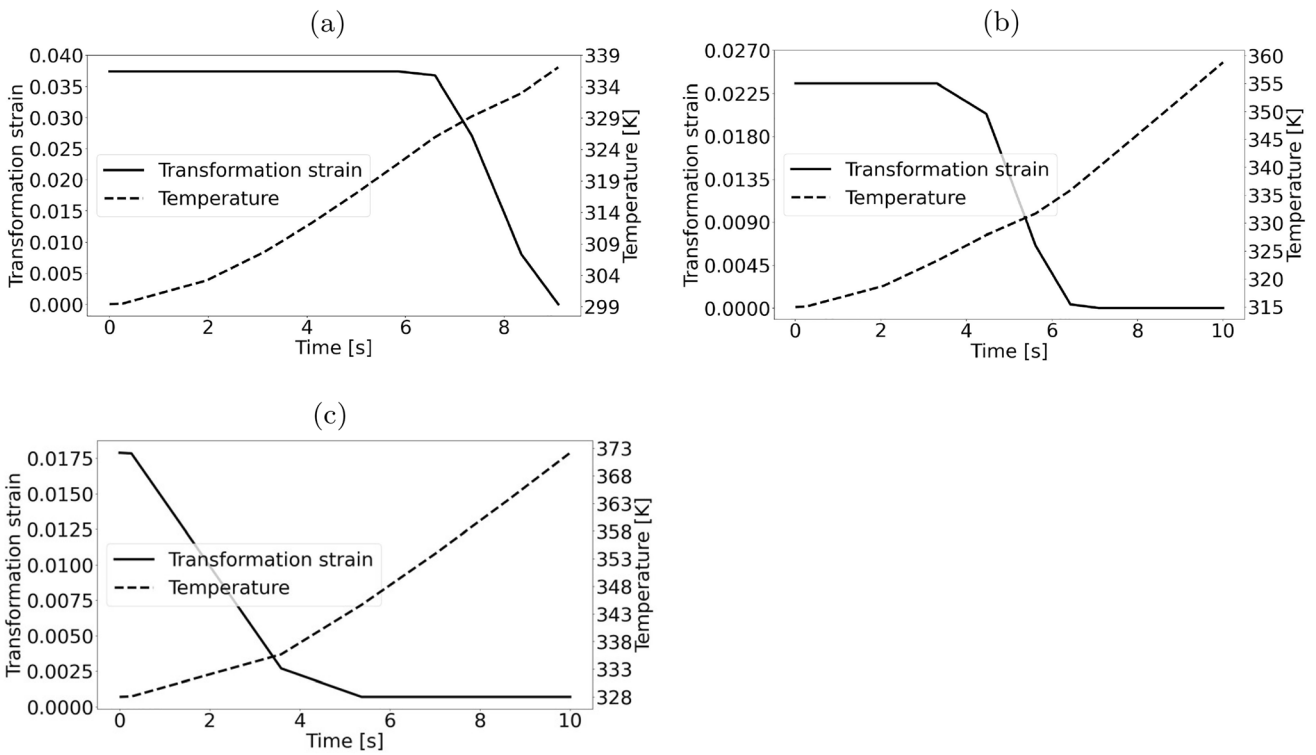

Fig. 8 Time-resolved FEM simulation of Joule heating and its effects on the temperature and transformation strain for reference temperatures: **a** 299 K, **b** 315 K, **c** 328 K

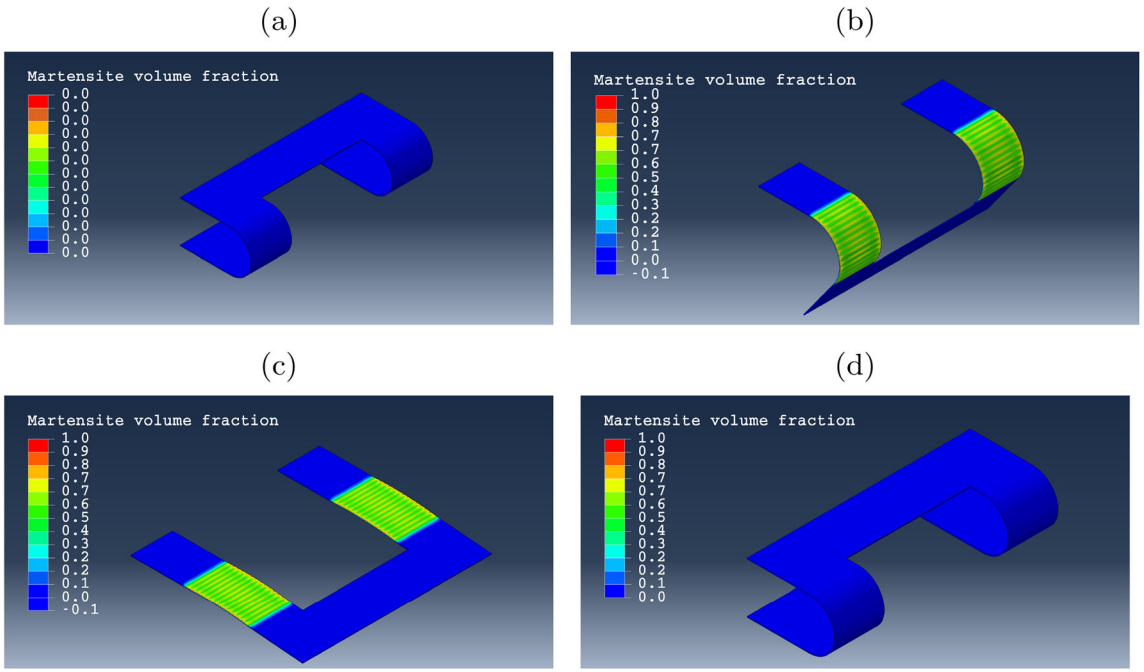

Fig. 9 Distribution of martensite volume fraction on the actuator surface during loading–unloading-Joule heating cycle, shown **a** for actuator in shape-set position; **b** after deflection to − 123°; **c** after elastically unloading to + 3°; **d** after recovery due to heating to the parent phase at + 180°

Bending Simulations

Here, FEM simulations consist of approximating the bending behavior of NiTi microactuators in no-load condition. The CAD geometry with dimensions of the bending microactuator can be found in Fig. 18 in Appendix 2. The actuator is in a shape-set configuration, that is, the memory shape determined by heat treatment above the austenite finish temperature, A_f. The experimental shape-setting procedure is explained in our previous work [19]. The vital region for actuation is the bent region. The heat-induced phase transformation of this region causes the actuation force or moment. Figure 9 shows the distribution of the stress-induced fraction of martensite. The actuator is bent from its shape-set configuration (Fig. 9a) to about −123° as seen in Fig. 9b and during elastic unloading as seen in Fig. 9c, the actuator deflects back to 3° because of the accumulated martensite phase. The actuator returns to it original shape-set configuration as seen in Fig. 9d, through Joule heating, whereby the temperature has increased to above austenite finish temperature, 335 K.

The phase transformation along the thickness of a bending actuator depends on the stress distribution. As the actuator unfolds from the original configuration (Fig. 9a and b), material layers above and below the neutral plane are subjected to tensile stresses and compressive stresses, respectively. In the neutral plane, the stress state is zero. This means, the material layers in the neutral plane do not transform. From the neutral plane, above and below, the

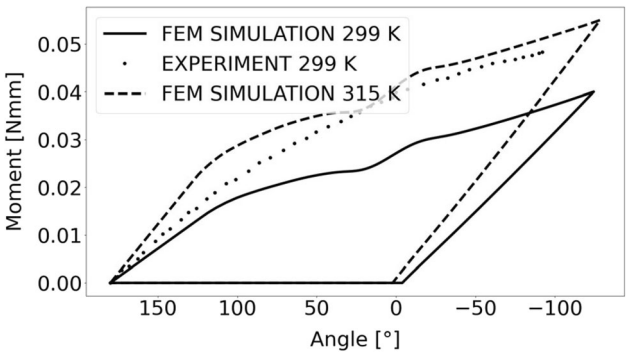

Fig. 10 Comparison of bending moment vs angle for experiment [19] and simulation

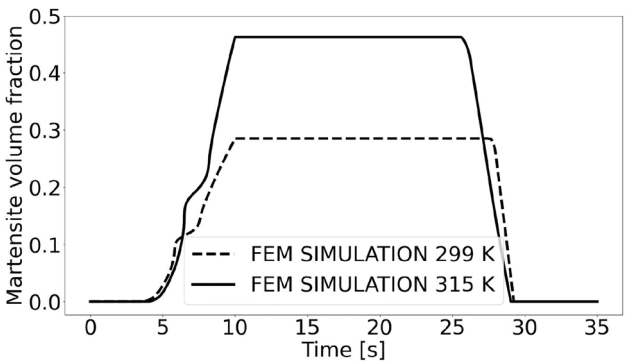

Fig. 11 Time-resolved evolution of the average martensite volume fraction

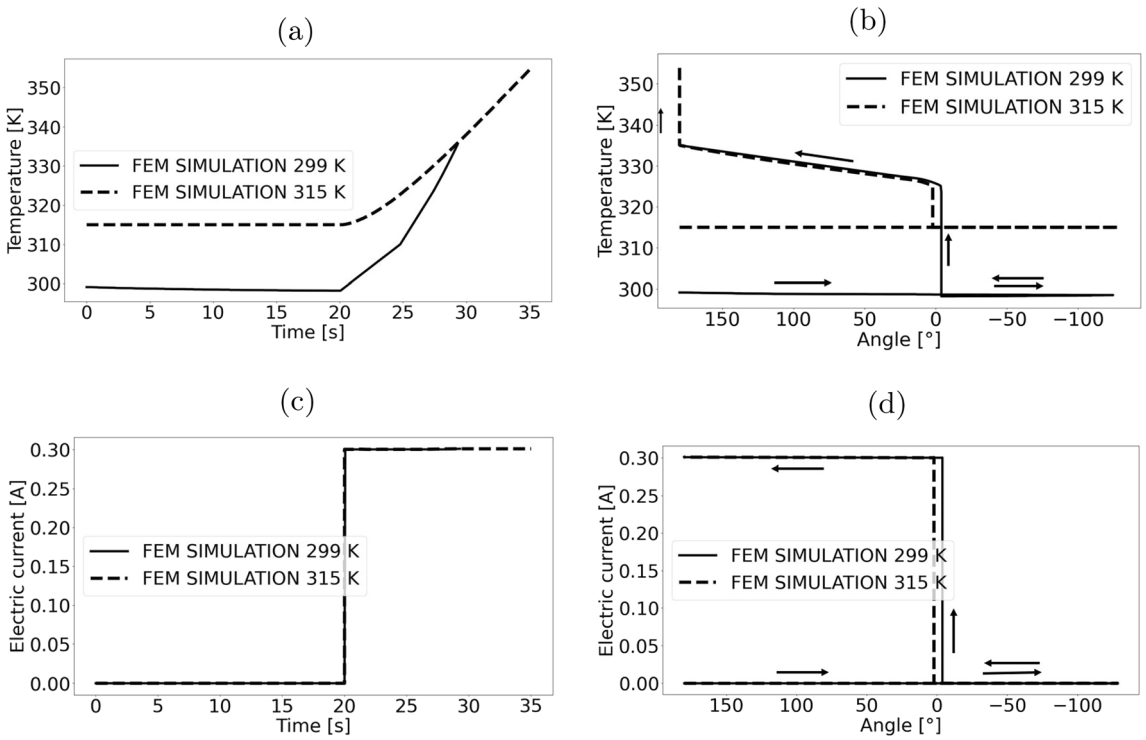

Fig. 12 Joule heating of the bending actuators at an electrical current of 0.3 A switched on after 20 s with 299 K and 315 K as reference temperature: **a** temperature–time diagram; **b** temperature–angle diagram; **c** electric current–time diagram; **d** electric current–angle diagram

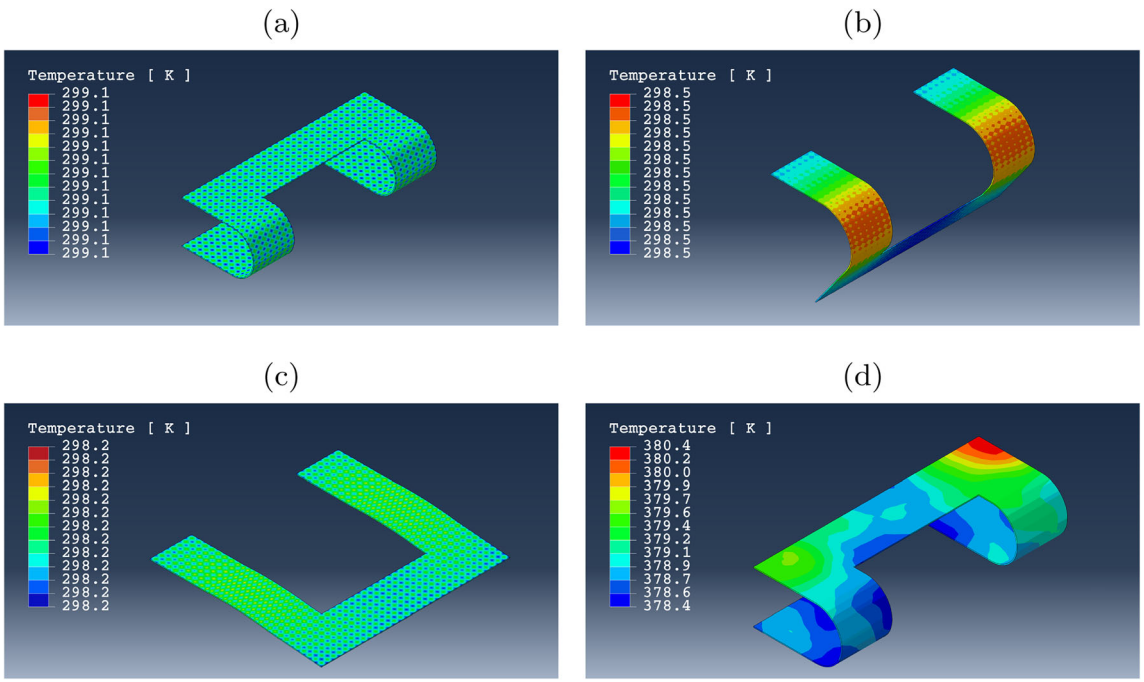

Fig. 13 Distribution of surface temperature for an actuator with initial temperature of 299 K and ambient temperature 298 K during loading–unloading-Joule heating cycle, shown for **a** shape-set position at + 180°; **b** after full bent to − 130°; **c** after full unloading to + 3°; **d** after recovery of the memory shape of + 180°

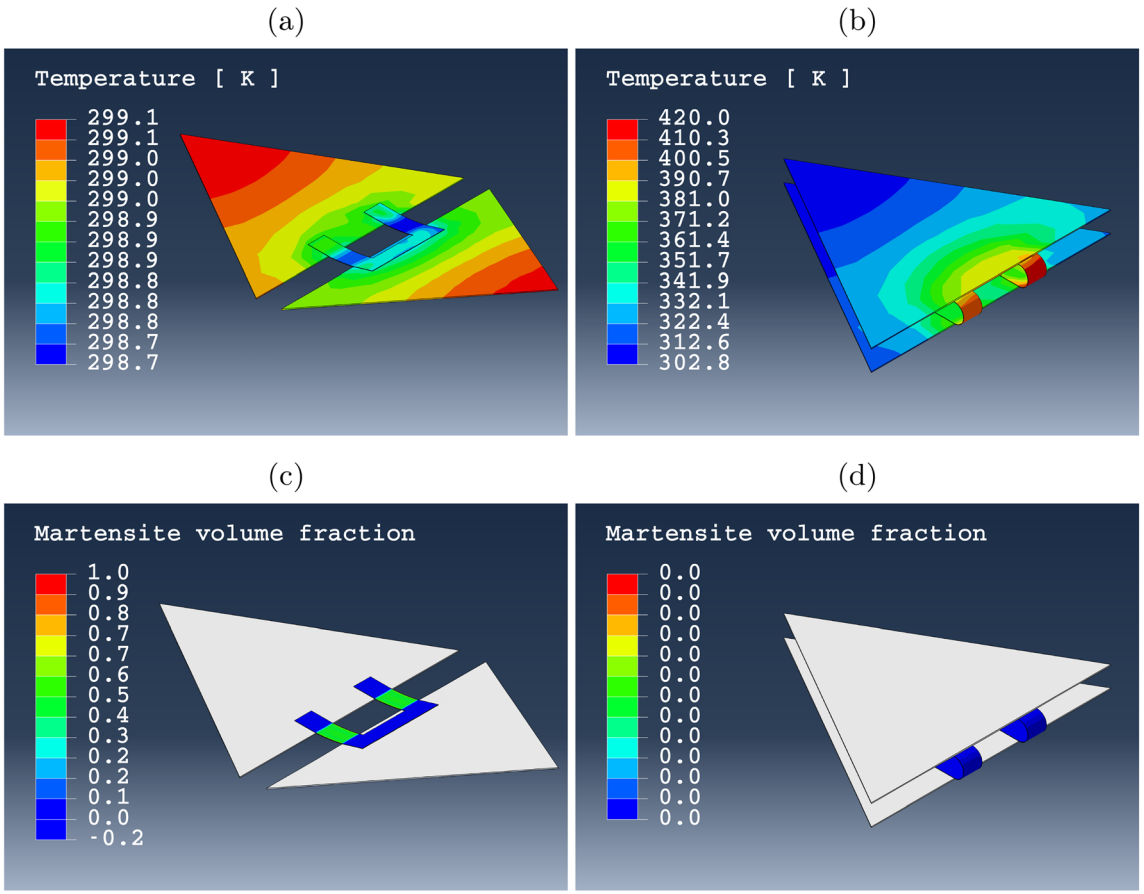

Fig. 14 Temperature and martensite fraction distribution during unidirectional bending actuation: **a** temperature distribution in initial actuation position at + 14°; **b** temperature distribution after complete phase transformation to + 180°; **c** martensite fraction distribution in initial actuation position at + 14°; **d** martensite fraction distribution after complete phase transformation to + 180°

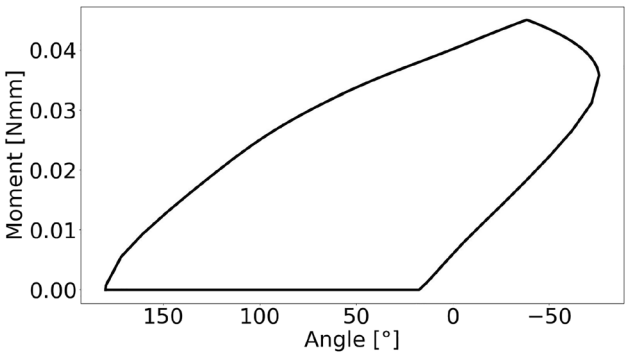

Fig. 15 Moment-angle diagram for unidirectional bending actuation

martensite transformation varies from $\xi = 0$ in the neutral plane to $\xi = 1$ at the top or bottom plane of the actuator. To observe such effects, the model is meshed with more than 2 finite elements across the thickness. Figure 10 shows a comparison between the experimental and simulation moment-angle diagrams at $T_{\text{ref}} = 299\,K$ and the simulated moment-angle diagram at $T_{\text{ref}} = 315\,K$. The discrepancy between experimental and simulated bending moment-angle values can be attributed to the tension-compression asymmetry of mechanical properties [53]. Compression leads to higher transformation stresses as compared to tension. This aspect is not included in the present model. The material properties are determined from tensile experiments.

Figure 11 shows the time-resolved evolution of the average fraction of martensite for both reference temperatures.

For shape recovery, a Joule heating simulation is conducted as part of the whole coupled simulation cycle. As seen in Fig. 12, after mechanical bending from + 180° to − 123°, a current is passed through the actuator (Fig. 12c and d). Due to the resistance of the actuator material, heat is dissipated. Consequently, the actuator's local temperature increases (Fig. 12a and b) and the actuator deflects back to the original shape-set configuration at 180° (Fig. 12d).

Figure 13 shows the corresponding temperature distribution across the actuator during loading (Fig. 13b), unloading (Fig. 13c) and Joule heating (Fig. 13d) from a reference temperature 299.1 K.

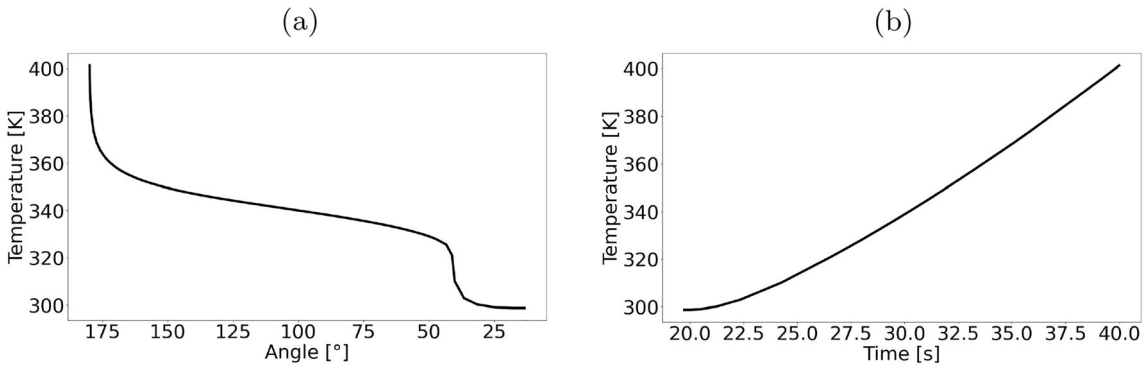

Fig. 16 Unidirectional bending actuation: **a** local temperature variation as a function of bending angle; **b** local temperature variation as a function of time

Unidirectional Bending Actuation

To show the capability of this model in actuation application, a unidirectional actuation simulation is carried out. The bending actuator is used to fold a triangular kapton tile through different angles based on the original shape-set configuration as seen in Fig. 20 in Appendix 2. The actuation is caused by Joule heating, which causes the actuator to deflect back to the original configuration. The purpose of such simulation is the determination of the actuation time and the heating power required for actuation. Unidirectional actuation means that during Joule heating the actuator will deflect the tile in one direction. The initial configuration for actuation is the position where the actuator has been elastically unloaded. Figure 14 shows the distribution of temperature (Fig. 14a and b) and martensite fraction (Fig. 14c and d) during unidirectional bending actuation. Because of the thermal conductivity of the kapton tile material, some energy is transferred to it, which increases the actuation time for the actuator.

Figure 15 shows the bending moment-angle diagram after a full loading-unloading-Joule heating simulation. After elastically unloading, a transformation angle of approximately 166° is induced. This is the starting point for unidirectional actuation.

In Fig. 16, a current of $0.4\,A$ is passed through the actuator. This corresponds to an energy density of $0.9\,J/mm^3$, 90% of which is converted into heat due to environmental heat losses. Within approximately 10 seconds, the local temperature is raised above the austenite finish transformation temperature of 335 K. This is the actuation time as seen in Fig. 16a and b. The triangular tile is deflected back to the original configuration at + 180°.

Conclusions

In this paper, a 3D electro-thermo-mechanical SMA material model is presented. The model captures the coupling effects between deformation and temperature during stress-induced phase transformation. In addition, the coupling effects between temperature and electrical potential are considered. This allows to simulate Joule heating, which is important in actuation of bending microactuators.

For model validation tensile test experiments of a 20 µm thin NiTi sample were simulated. A comparative study of the simulation and experimental results was conducted. Stress levels were approximated within acceptable range. Two strain rates were simulated to study their effects on the temperature variation during stress-induced phase transformation. These effects were quantified in form of temperature–time diagrams. Slight deviation were observed regarding the temperature between the simulation and experimental results. We observed higher temperature levels in simulation results as compared to experimental results due to additional heat transfer to the supporting substrate. We also observed the sensitivity of these results to the thermal parameters. Finally, the full loading–unloading-Joule heating simulation was conducted for three different temperature levels. Here, the effect of temperature changes, due to Joule heating, on the internal state variables was reported.

To show the capability of the presented material model in bending-dominated problems, bending simulations of microactuators were conducted and compared with experimental results. Simulation results on the martensite fraction and temperature variable was reported for the full loading–unloading-heating cycle. A comparison between bending moment versus rotation angle of the simulation and experimental results for a reference temperature of 299 K was conducted.

An initial demonstration of microactuation application was presented. Unidirectional actuation of a triangular tile was conducted. Data relevant for the prediction of the physical actuation set-up were presented. Actuation time, actuation current, optimal model geometry can therefore be obtained with the presented material model.

Considering the aforementioned simulation results, we conclude that the presented material model can be used to

simulate the electro-thermo-mechanical behavior of 3D SMA materials during tensile or bending loading.

Appendix 1: Finite Element Formulation

Rewriting the governing partial differential equations decribing the mechanical, thermal, and electrical problems as presented in Eqs. (4) and (22) respectively, gives

$$\begin{aligned} &\nabla \cdot \boldsymbol{\sigma} + \boldsymbol{b} = 0 \\ &\rho c \dot{T} - \nabla \cdot (\boldsymbol{q}) = H_{\text{elec}} - T \frac{\partial \pi}{\partial T} \dot{\xi} + d_{\text{mec}} \\ &\nabla \cdot \boldsymbol{J} - r_c = 0 \end{aligned} \tag{31}$$

Obtaining the weak form of the governing equations by multiplying the above equations by suitable variational test fields, δu for the displacement, δT for the temperature, and δv for the electric potential and integrating over the volume, results in

$$\begin{aligned} &\int_V \delta u \nabla \cdot \boldsymbol{\sigma}(\varepsilon)\, \mathrm{d}V + \int_V \delta u \mathbf{b}\, \mathrm{d}V = 0 \\ &\int_V \delta T \rho c \dot{T}\, \mathrm{d}V - \int_V \delta T\, \nabla \cdot (\mathbf{q})\, \mathrm{d}V = \int_V \delta T H_{\text{elec}}\, \mathrm{d}V \\ &\quad - \int_V \delta T T \frac{\partial \pi}{\partial T} \dot{\xi}\, \mathrm{d}V + \int_V \delta T d_{\text{mec}}\, \mathrm{d}V \\ &\int_V \delta v \nabla \cdot \boldsymbol{J}\, \mathrm{d}V - \int_V \delta v r_c\, \mathrm{d}V = 0 \end{aligned} \tag{32}$$

Note here that for an hypoeleastic material, the stress tensor is a non-linear function of strain, $\sigma(\varepsilon)$, applying the chain rule and then the divergence theorem on the term with the gradient operator,

$$\begin{aligned} &\int_V \nabla \delta u \cdot \boldsymbol{\sigma}(\varepsilon)\, \mathrm{d}V - \int_S \delta u\, \boldsymbol{\sigma} \cdot \mathbf{n}\, \mathrm{d}S + \int_V \delta u \mathbf{b}\, \mathrm{d}V = 0 \\ &\int_V \nabla \delta T \cdot (\mathbf{q})\, \mathrm{d}V + \int_S \delta T\, \boldsymbol{q} \cdot \boldsymbol{n}\, \mathrm{d}S - \int_V \delta T\, \rho c \dot{T}\, \mathrm{d}V \\ &\quad + \int_V \delta T\, H_{\text{elec}}\, \mathrm{d}V - \int_V \delta T\, T \frac{\partial \pi}{\partial T} \dot{\xi}\, \mathrm{d}V \\ &\quad + \int_V \delta T\, d_{\text{mec}}\, \mathrm{d}V = 0 \\ &\int_V \nabla \delta v \cdot \boldsymbol{J}\, \mathrm{d}V + \int_S \delta v \boldsymbol{J} \cdot \boldsymbol{n}\, \mathrm{d}S - \int_V \delta v\, r_c\, \mathrm{d}V \end{aligned} \tag{33}$$

To obtain the spatial discretization of the volume of the solid, the displacement, the temperature, and the electric potential are calculated at a set of nodes whose coordinates is x^a where a ranges from 1 to n. These discrete points are u^a, T^a, and v^a for the displacement, temperature, and electric potential, respectively. By interpolating between these nodal values, the approximated field values at the finite element level are obtained, the interpolation functions are defined below,

$$\begin{aligned} u(x) &= N^a(x) u^a \quad \delta u(x) = N^a(x) \delta u^a \\ T(x) &= N^a(x) T^a \quad \delta T(x) = N^a(x) \delta T^a \\ v(x) &= N^a(x) v^a \quad \delta v(x) = N^a(x) \delta v^a \end{aligned} \tag{34}$$

where N^a, $(\delta u)^a$, $(\delta T)^a$, $(\delta v)^a$ are the interpolatioin function, the virtual displacement, the virtual temperature, and the virtual electric potential at node a. Adopting Einstein summation convention over the superscript a for n number of nodes on the element. Substituting the interpolation functions in Eq. (33) gives

$$\begin{aligned} &\int_V \nabla N^a(x) \delta u^a \cdot \boldsymbol{\sigma}(\varepsilon)\, \mathrm{d}V - \int_S N^a(x) \delta u^a\, \boldsymbol{\sigma} \cdot \mathbf{n}\, \mathrm{d}S \\ &\quad + \int_V N^a(x) \delta u^a \boldsymbol{b}\, \mathrm{d}V = 0 \\ &\int_V \nabla N^a(x) \delta T^a \cdot (\boldsymbol{q})\, \mathrm{d}V + \int_S N^a(x) \delta T^a\, \boldsymbol{q} \cdot \mathbf{n}\, \mathrm{d}S \\ &\quad - \int_V N^a(x) \delta T^a\, \rho c \dot{T}\, \mathrm{d}V + \int_V N^a(x) \delta T^a\, H_{\text{elec}}\, \mathrm{d}V \\ &\quad - \int_V N^a(x) \delta T^a\, N^a(x) T^a \frac{\partial \pi}{\partial T} \dot{\xi}\, \mathrm{d}V \\ &\quad + \int_V N^a(x) \delta T^a\, d_{\text{mec}}\, \mathrm{d}V = 0 \\ &\int_V \nabla N^a(x) \delta v^a \cdot \mathbf{J}\, \mathrm{d}V + \int_S N^a(x) \delta v^a\, \mathbf{J} \cdot \mathbf{n}\, \mathrm{d}S \\ &\quad - \int_V N^a(x) \delta v^a\, r_c\, \mathrm{d}V = 0 \end{aligned} \tag{35}$$

Eliminating the corresponding virtual quantities in all three equation gives

$$\begin{aligned} &\int_V \nabla N^a(x) \cdot \boldsymbol{\sigma}(\varepsilon)\, \mathrm{d}V - \int_S N^a(x)\, \boldsymbol{\sigma} \cdot \mathbf{n}\, \mathrm{d}S \\ &\quad + \int_V N^a(x) \mathbf{b}\, \mathrm{d}V = 0 \\ &\int_V \nabla N^a(x) \cdot (\mathbf{q})\, \mathrm{d}V + \int_S N^a(x)\, \boldsymbol{q} \cdot \mathbf{n}\, \mathrm{d}S \\ &\quad - \int_V N^a(x)\, \rho c \dot{T}\, \mathrm{d}V + \int_V N^a(x)\, H_{\text{elec}}\, \mathrm{d}V \\ &\quad - \int_V N^a(x)\, N^a(x) T^a \frac{\partial \pi}{\partial T} \dot{\xi}\, \mathrm{d}V + \int_V N^a(x)\, d_{\text{mec}}\, \mathrm{d}V = 0 \\ &\int_V \nabla N^a(x) \cdot \mathbf{J}\, \mathrm{d}V + \int_S N^a(x) \boldsymbol{J} \cdot \mathbf{n}\, \mathrm{d}S \\ &\quad - \int_V N^a(x)\, r_c\, \mathrm{d}V = 0 \end{aligned} \tag{36}$$

The time derivatives are approximated using the backward Euler method such that

$$\dot{\xi} = \frac{\xi^{t+\Delta t} - \xi^t}{\Delta t} \tag{37}$$

for the martensite volume fraction and

$$\dot{T} = \frac{T^{t+\Delta t} - T^t}{\Delta t} \tag{38}$$

for the temperature are obtained. Substituting this expression in Eq. (36) gives

$$\begin{aligned}
&\int_V \nabla N^a(x) \cdot \boldsymbol{\sigma}(\varepsilon)\ \mathrm{d}V - \int_S N^a(x)\,\boldsymbol{\sigma} \cdot \mathbf{n}\ \mathrm{d}S \\
&\quad + \int_V N^a(x)\mathbf{b}\ \mathrm{d}V = 0 \\
&\int_V \nabla N^a(x) \cdot (\mathbf{q})\ \mathrm{d}V + \int_S N^a(x)\,\boldsymbol{q} \cdot \boldsymbol{n}\ \mathrm{d}S \\
&\quad - \int_V N^a(x)\,\rho c \left(\frac{T^{t+\Delta t} - T^t}{\Delta t}\right) \mathrm{d}V + \int_V N^a(x)\,H_{\mathrm{elec}}\ \mathrm{d}V \\
&\quad - \int_V N^a(x)\,N^a(x) T^a \frac{\partial \pi}{\partial T} \left(\frac{\xi^{t+\Delta t} - \xi^t}{\Delta t}\right) \mathrm{d}V \\
&\quad + \int_V N^a(x)\,d_{\mathrm{mec}}\ \mathrm{d}V = 0 \\
&\int_V \nabla N^a(x) \cdot \boldsymbol{J}\ \mathrm{d}V + \int_S N^a(x)\,\boldsymbol{J} \cdot \mathbf{n}\ \mathrm{d}S \\
&\quad - \int_V N^a(x)\,r_c\ \mathrm{d}V = 0
\end{aligned} \tag{39}$$

The next step in the formulation is the evaluation of the integral. Gauss quadrature is the most efficient numerical method to evaluate these continuous integrals by replacing them with finite sums. After mapping the global coordinates $\{x, y, z\}$ to the local element coordinates $\{g, h, r\}$, each of which spans $\{-1,+1\}$ in an element. For 3D problems, the coordinate mapping and Gauss quadrature are

$$\begin{aligned}
&x(g,h,r) = N^a(g,h,r)x^a \\
&y(g,h,r) = N^a(g,h,r)y^a \\
&z(g,h,r) = N^a(g,h,r)z^a \\
&\mathrm{d}x\,\mathrm{d}y\,\mathrm{d}z = J\,\mathrm{d}g\,\mathrm{d}h\,\mathrm{d}r \\
&J = \begin{bmatrix} \frac{\partial x}{\partial g} & \frac{\partial y}{\partial g} & \frac{\partial z}{\partial g} \\ \frac{\partial x}{\partial h} & \frac{\partial y}{\partial h} & \frac{\partial z}{\partial h} \\ \frac{\partial x}{\partial r} & \frac{\partial y}{\partial r} & \frac{\partial z}{\partial r} \end{bmatrix} \\
&\int_{-1}^{+1}\int_{-1}^{+1}\int_{-1}^{+1} f(g,h,r)det[J(g,h,r)]\,\mathrm{d}g\,\mathrm{d}h\,\mathrm{d}r \\
&\quad = \sum_{i=1}^{ngp}\sum_{j=1}^{ngp}\sum_{k=1}^{ngp} w_i w_j w_k f(g_i,h_j,r_k) det[J(g_i,h_j,r_k)]
\end{aligned} \tag{40}$$

where ngp is the number of Gauss integration points, w_i are the integration weights, and J is the Jacobian of coordinates transformation.

Appendix 2: CAD Geometric Models

See Figs. 17, 18, 19, 20, and 21.

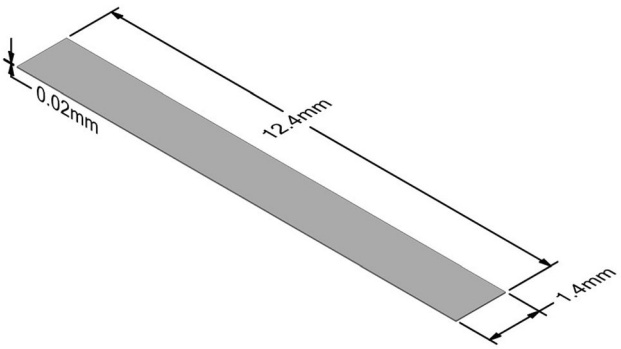

Fig. 17 Tensile sample

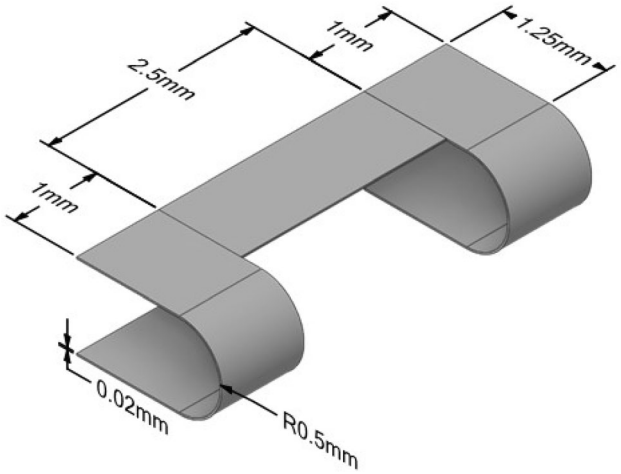

Fig. 18 SMA bending microactuator in shape-set configuration (no-load condition: no tile attached)

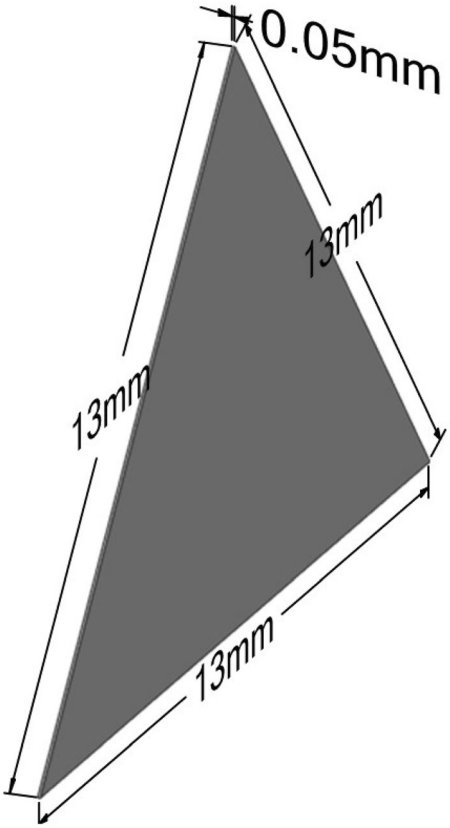

Fig. 19 Actuated tile

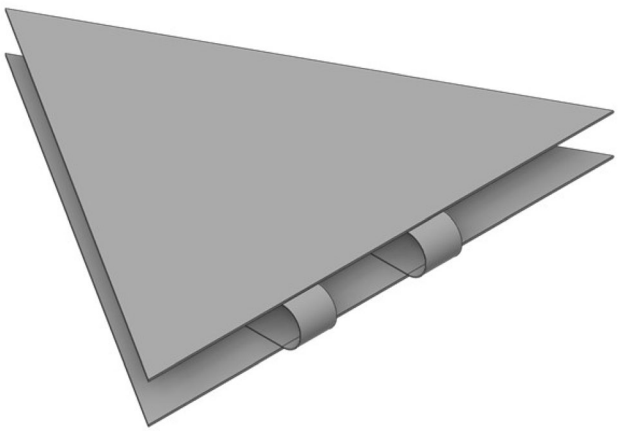

Fig. 20 Actuator-tile assembly (load-condition)

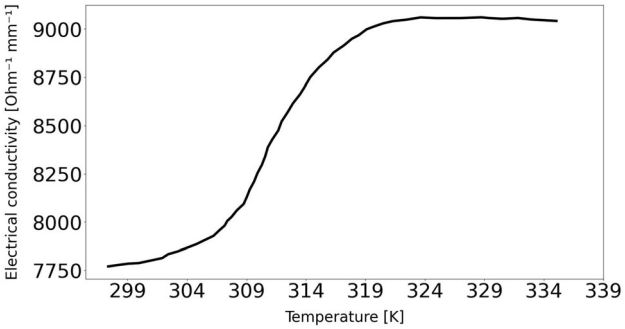

Fig. 21 Temperature dependent conductivity [19]

Appendix 3: Material Model Parameters

Please note that unless experimentally measured, the initial internal energy Δu_0 and initial entropy Δs_0 are set to zero. Experimentally, for room temperature, it was observed that the martensite stiffness, E_M, was higher than that of the parent phase stiffness, E_P, the R-phase. This relation changes for higher temperatures. To compute the critical stresses, the following equations are used:

$$\begin{aligned} \sigma_{scr} &= \sigma_s - C^{PM} \cdot (T_{ref} - M_s) \\ \sigma_{fcr} &= \sigma_f - C^{MP} \cdot (T_{ref} - M_s) \end{aligned} \tag{41}$$

The stress values marking the start and the end of the transformation bands, σ_s and σ_f, respectively, are obtained from the characterization data. The critical stress can be computed individually for each testing temperature using the above-mentioned equations. This is necessary for uncertain values of the Clausius–Clayperon coefficients. Due to caloric effects, T_{ref} varies. This changes the value of σ_{fcr}, which is used for approximation of the plateau region. Attention should be paid here by calculating the temperature gradient during transformation and correspondingly compute σ_{fcr}. A temperature-dependent electrical conductivity is used as seen in the Fig. 21. Simulation parameters are summarized in Tables 1, 2 and 3.

Table 1 Parameters for tensile and bending simulation at $T_{ref} = 299$ K

Property	Value	References
Mechanical parameters		
Critical start and finish stress, $\sigma_{scr}, \sigma_{fcr}$	56, 225, MPa	[19]
Clausius Clapeyron coefficient C^{AM}, C^{MA}	6.6, 6.6 MPa K^{-1}	[19]
Maximum transformation strain, ϵ^{tr}_{max}	0.037	[19]
Young Modulus E^A, E^M	12500, 20500, MPa	[19]
Poisson ratio, μ^A, μ^M	0.33,0.33	–
Martensite finish and start temperature, Mf ,Ms	282, 292 K	[19]
Austenite start and finish, As, Af	325, 335 K	[19]
Heat capacity , c^A, c^M	3612.3, 3612.3 J kg^{-1} K^{-1}	[50]
Δs_0	0 J Kg^{-1} K^{-1}	
Δu_0	0 J kg^{-1}	
Material density, ρ	6.45E^{-6} kg mm^{-3}	
Thermal parameters		
Thermal conductivity	0.0055 W mm^{-1} K^{-1}	[50]
Heat capacity , c	3612.3 J kg^{-1} K^{-1}	[50]
Process parameters		
Ambient temperature T_{amb}	299, 299 K	[19]
Reference temperature T_{ref}	299.14, 299.44 K	[19]
Convection coefficient	6.6405E−05 W mm^{-2} K^{-1}	[51]
Strain rate	$5 \times 10^{-1}s^{-1}, 10^{-2}s^{-1}$	–

Table 2 Parameters for tensile and bending simulation at $T_{ref} = 315$ K

Property	Value	References
Mechanical parameters		
Critical start and finish stress, $\sigma_{scr}, \sigma_{fcr}$	56, 181.6, MPa	[19]
Clausius Clapeyron coefficient C^{AM}, C^{MA}	3.4, 3.4 MPa K^{-1}	[19]
Maximum transformation strain, ϵ^{tr}_{max}	0.0245	[19]
Young Modulus E^A, E^M	21428, 18000, MPa	[19]
Poisson ratio, μ^A, μ^M	0.33,0.33	–
Martensite finish and start temperature, Mf ,Ms	282, 292 K	[19]
Austenite start and finish, As, Af	325, 335 K	[19]
Heat capacity , c^A, c^M	3612.3, 3612.3 J kg^{-1} K^{-1}	[50]
Δs_0	0 J kg^{-1} K^{-1}	
Δu_0	0 J kg^{-1}	
Material density, ρ	6.45E^{-6} Kg mm^{-3}	–
Thermal parameters		
$^{-1}$Thermal conductivity	0.0055 W mm^{-1} K^{-1}	[50]
Heat capacity, c	3612.3 J kg^{-1} K^{-1}	[50]
Process parameters		
Ambient temperature T_{amb}	315 K	[19]
Reference initial temperature T_{ref}	315 K	[19]
Convection coefficient	6.6405E−05 W mm^{-2} K^{-1}	[51]
Strain rate	10^{-4} s^{-1}	–

Table 3 Parameters for tensile and bending simulation at $T_{ref} = 328$ K

Property	Value	References
Mechanical parameters		
Critical start and finish stress, $\sigma_{scr}, \sigma_{fcr}$	56, 125.4, MPa	[19]
Clausius Clapeyron coefficient C^{AM}, C^{MA}	5.1, 5.1 MPa K^{-1}	[19]
Maximum transformation strain, ϵ^{tr}_{max}	0.0175	[19]
Young Modulus E^A, E^M	24333, 15,000, MPa	[19]
Poisson ratio, μ^A, μ^M	0.33,0.33	–
Martensite finish and start temperature, Mf ,Ms	282, 292 K	[19]
Austenite start and finish, As, Af	325, 335 K	[19]
Heat capacity , c^A, c^M	3612.3, 3612.3 J kg^{-1} K^{-1}	[50]
Δs_0	0 J kg^{-1} K^{-1}	
Δu_0	0 J kg^{-1}	
Material density, ρ	6.45E^{-06} kg mm^{-3}	–
Thermal parameters		
Thermal conductivity	0.0055 W mm^{-1} K^{-1}	[50]
Heat capacity , c	3612.3 J kg^{-1} K^{-1}	[50]
Process parameters		
Ambient temperature T_{amb}	328 K	[19]
Reference initial temperature T_{ref}	328 K	[19]
Convection coefficient	6.6405E−05 W mm^{-2} K^{-1}	[51]
Strain rate	$10^{-4}s^{-1}$	–

Acknowledgements The authors acknowledge the project funding by the German Research Foundation (Deutsche Forschungsgemeinschaft, DFG) within the priority program "Cooperative Multistage Multistable Microactuator Systems".

Funding Open Access funding enabled and organized by Projekt DEAL.

Data Availability The user-defined material subroutine and the corresponding input files used in the presented work are available to download from the GitHub: https://simlab.ww.uni-erlangen.de/functionalmaterials/coupledfem_smasimulations

References

1. Buehler WJ, Gilfrich JV, Wiley RC (1963) Effect of low-temperature phase changes on the mechanical properties of alloys near composition TiNi. J Appl Phys 34(5):1475–1477
2. Wang FE, Buehler WJ, Pickart SJ (1965) Crystal structure and a unique martensitic transition of TiNi. J Appl Phys 36(10):3232–3239
3. Ryhänen J (2000) Biocompatibility of Nitinol. Minim Invasive Therapy Allied Technol 9(2):99–105
4. Hornbogen E (1990) Thermo-mechanical fatigue of shape memory alloys. In: Herrmann KP, Olesiak ZS (eds) Thermal effects in fracture of multiphase materials. Springer, Heidelberg, pp 156–167
5. Hodgson DE (2001) Damping applications of shape-memory alloys. Mater Sci Forum 394:69–74
6. Qian L, Xiao X, Sun Q, Yu T (2004) Anomalous relationship between hardness and wear properties of a superelastic Nickel–Titanium alloy. Appl Phys Lett 84(7):1076–1078
7. Luo Y, Li D (2001) New wear-resistant material: nano-TiN–TiC–TiNi composite. J Mater Sci 36(19):4695–4702
8. Ikuta K (1990) Micro/miniature shape memory alloy actuator. In: Proceedings IEEE international conference on robotics and automation, IEEE. pp 2156–2161
9. Kohl M (2004) Shape memory microactuators. Springer, Heidelberg
10. Kohl M, Ossmer H, Gueltig M, Megnin C (2018) SMA foils for MEMS: from material properties to the engineering of microdevices. Shape Memory Superelast 4(1):127–142
11. Kahn H, Huff MA, Heuer AH (1998) The TiNi shape-memory alloy and its applications for mems. J Micromech Microeng 8(3):213
12. Benard WL, Kahn H, Heuer A, Huff MA (1997) A titanium–nickel shape-memory alloy actuated micropump. In: Proceedings of international solid state sensors and actuators conference (transducers' 97), IEEE. vol 1, pp 361–364
13. Gill JJ, Chang DT, Momoda LA, Carman GP (2001) Manufacturing issues of thin film NiTi microwrapper. Sens Actuators A 93(2):148–156

14. Miyazaki S, Fu YQ, Huang WM (2009) Thin film shape memory alloys: fundamentals and device applications. Cambridge University Press, Cambridge
15. Hahm G (2001) Microfabricated, silicon spring biased, shape memory actuated microvalve. Case Western Reserve University, Cleveland
16. Lai B-K, Hahm G, You L, Shih C-L, Kahn H, Phillips S, Heuer A (2000) The characterization of TiNi shape-memory actuated microvalves. MRS Online Proceedings Library (OPL) 657
17. Stepan LL, Levi DS, Carman GP (2005) A thin film nitinol heart valve
18. Hawkes E, An B, Benbernou NM, Tanaka H, Kim S, Demaine ED, Rus D, Wood RJ (2010) Programmable matter by folding. Proc Natl Acad Sci 107(28):12441–12445
19. Seigner L, Tshikwand GK, Wendler F, Kohl M (2021) Bi-directional origami-inspired SMA folding microactuator. Actuators 10:181
20. Tanaka K, Kobayashi S, Sato Y (1986) Thermomechanics of transformation pseudoelasticity and shape memory effect in alloys. Int J Plast 2(1):59–72
21. Brinson LC (1993) One-dimensional constitutive behavior of shape memory alloys: thermomechanical derivation with non-constant material functions and redefined martensite internal variable. J Intell Mater Syst Struct 4(2):229–242
22. Boyd JG, Lagoudas DC (1996) A thermodynamical constitutive model for shape memory materials. Part I. the monolithic shape memory alloy. Int J Plast 12(6):805–842
23. Boyd JG, Lagoudas DC (1996) A thermodynamical constitutive model for shape memory materials. Part II. The SMA composite material. Int J Plast 12(7):843–873
24. Xu L, Baxevanis T, Lagoudas D (2019) A three-dimensional constitutive model for the martensitic transformation in polycrystalline shape memory alloys under large deformation. Smart Mater Struct 28(7):074004
25. Xu L, Solomou A, Baxevanis T, Lagoudas D (2021) Finite strain constitutive modeling for shape memory alloys considering transformation-induced plasticity and two-way shape memory effect. Int J Solids Struct 221:42–59
26. Patoor E, Lagoudas DC, Entchev PB, Brinson LC, Gao X (2006) Shape memory alloys, Part I: general properties and modeling of single crystals. Mech Mater 38(5–6):391–429
27. Lagoudas DC, Entchev PB, Popov P, Patoor E, Brinson LC, Gao X (2006) Shape memory alloys, Part II: modeling of polycrystals. Mech Mater 38(5–6):430–462
28. Jaber MB, Smaoui H, Terriault P (2008) Finite element analysis of a shape memory alloy three-dimensional beam based on a finite strain description. Smart Mater Struct 17(4):045005
29. Alsawalhi MY, Landis CM (2021) A new phenomenological constitutive model for shape memory alloys. Int J Solids Struct. https://doi.org/10.1016/j.ijsolstr.2021.111319
30. Scalet G, Niccoli F, Garion C, Chiggiato P, Maletta C, Auricchio F (2019) A three-dimensional phenomenological model for shape memory alloys including two-way shape memory effect and plasticity. Mech Mater 136:103085
31. Lagoudas DC (ed) (2008) Shape memory alloys: modeling and engineering applications. Springer, New York
32. Lehmann T (1980) Coupling phenomena in thermoplasticity. Nucl Eng Des 57(2):323–332
33. Andrzej Łużalec S (1990) An evaluation of the internal dissipation factor in coupled thermoplasticity. Int J Non-Linear Mech 25(4):395–403
34. Bruhns O, Służalec A (1989) Thermal effects in thermoplastic metal with internal variables. Comput Struct 33(6):1459–1464
35. Antonucci V, Auricchio F, Lecce L, Sacco E et al (2021) Shape memory alloy engineering: for aerospace, structural, and biomedical applications. Butterworth-Heinemann, Oxford
36. Yu C, Kang G, Kan Q, Zhu Y (2015) Rate-dependent cyclic deformation of super-elastic NiTi shape memory alloy: thermo-mechanical coupled and physical mechanism-based constitutive model. Int J Plast 72:60–90
37. Xu R, Bouby C, Zahrouni H, Zineb TB, Hu H, Potier-Ferry M (2018) 3D modeling of shape memory alloy fiber reinforced composites by multiscale finite element method. Compos Struct 200:408–419
38. Frost M, Jury A, Heller L, Sedlák P (2021) Experimentally validated constitutive model for NiTi-based shape memory alloys featuring intermediate r-phase transformation: A case study of Ni48Ti49Fe3. Mater Design 203:109593
39. Coleman B, Noll W (1963) The thermodynamics of elastic materials with heat conduction. Arch Ration Mech Anal 13:167
40. Gurtin ME, Fried E, Anand L (2010) The mechanics and thermodynamics of continua. Cambridge University Press, Cambridge
41. Raniecki B, Lexcellent C (1994) Rl-models of pseudoelasticity and their specification for some shape memory solids. Eur J Mech A 13(1):21–50
42. Sun QP, Hwang KC (1993) Micromechanics modelling for the constitutive behavior of polycrystalline shape memory alloys—I. derivation of general relations. J Mech Phys Solids 41(1):1–17
43. Sun QP, Hwang KC (1993) Micromechanics modelling for the constitutive behavior of polycrystalline shape memory alloys—II. Study of the individual phenomena. J Mech Phys Solids 41(1):19–33
44. Smith M (2009) ABAQUS/Standard User's Manual, Version 6.9. Dassault Systèmes Simulia Corp, United States
45. Nagtegaal JC (1982) On the implementation of inelastic constitutive equations with special reference to large deformation problems. Comput Methods Appl Mech Eng 33(1–3):469–484
46. Hughes TJ, Winget J (1980) Finite rotation effects in numerical integration of rate constitutive equations arising in large-deformation analysis. Int J Numer Meth Eng 15(12):1862–1867
47. Bathe K-J, Ramm E, Wilson EL (1975) Finite element formulations for large deformation dynamic analysis. Int J Numer Meth Eng 9(2):353–386
48. Bathe K-J, Bolourchi S (1979) Large displacement analysis of three-dimensional beam structures. Int J Numer Meth Eng 14(7):961–986
49. Wilkins ML (1963) Calculation of elastic-plastic flow. Technical report, California Univ Livermore Radiation Lab
50. Welsch F, Ullrich J, Ossmer H, Schmidt M, Kohl M, Chluba C, Quandt E, Schütze A, Seelecke S (2018) Numerical simulation and experimental investigation of the elastocaloric cooling effect in sputter-deposited tinicuco thin films. Continuum Mech Thermodyn 30(1):53–68
51. Bhattacharyya A, Sweeney L, Faulkner M (2002) Experimental characterization of free convection during thermal phase transformations in shape memory alloy wires. Smart Mater Struct 11(3):411
52. Wendler F, Ossmer H, Chluba C, Quandt E, Kohl M (2017) Mesoscale simulation of elastocaloric cooling in SMA films. Acta Mater 136:105–117
53. Kim Y-J, Lee C-H, Kim J-H, Lim JH (2018) Numerical modeling of shape memory alloy plates considering tension/compression asymmetry and its verification under pure bending. Int J Solids Struct 136:77–88